Journal of Solid State Chemistry **145,** 517–540 (1999)
Article ID jssc.1999.8200, available online at http://www.idealibrary.com on IDEAL®

Empirical Potentials for Modeling Solids, Surfaces, and Clusters

Hazel Cox,* Roy L. Johnston,† and John N. Murrell*

*School of Chemistry, Physics and Environmental Sciences, University of Sussex, Falmer, Brighton, BN1 9QJ, United Kingdom; and
†School of Chemistry, University of Birmingham, Edgbaston, Birmingham, B15 2TT, United Kingdom
*E-mail: kafg3@tc.mols.susx.ac.uk; †E-mail: roy@tc.bham.ac.uk

Received September 29, 1998; in revised form January 26, 1999; accepted February 2, 1999

A review of studies that have been made using the Murrell–Mottram two-plus-three-body empirical potential is presented. The explicit many-body nature of the potential is described and the fitting of these potentials to experimental data on one or more solid phases is detailed. Comparisons are made between potentials for various nonmetallic and metallic elements, from which trends in the parameters defining the potentials can clearly be seen. Examples of the many applications of these potentials to the study of solids (relative stabilities and phase transitions), surfaces (energies, relaxation and reconstructions), melting (both of the bulk and of the surfaces), and clusters (structures, growth, and dynamics) are given. © 1999 Academic Press

1. INTRODUCTION

The structures of atomic solids, their phase transformations, their surface and defect characteristics, the nature of their microclusters, and their melting behavior all provide a rich source for experimental and theoretical studies. A question examined in many papers has been whether a potential energy function for the atomic interactions can rationalize the experimental findings. The origins of this potential, and the difference between one atom and another, lie in the electrons, in particular, how they interact with the nuclei and with one another; as with molecules, we can adopt the Born–Oppenheimer approximation and seek to find an interatomic potential which controls the structure and atom dynamics of the system.

It is important at this point to note a significant difference between molecular and solid state potentials. Most molecules have electronic states which are well separated in energy, and the interatomic potential is electronic state specific (this is clearly encompassed in the Born–Oppenheimer approximation); different electronic states will usually have quite different potentials. Most atomic solids in contrast are metals, the major exceptions being the Group 14 solids and the inert gases, and metals have a continuum of electronic levels whose population varies with temperature. Hence, if an interatomic potential were defined to represent a structure at absolute zero, we would certainly expect this potential to fail to some extent at the melting point of the metal; we do not know how badly it fails but some indication would be given by examining the change in the experimental phonon frequencies on passing from absolute zero to the melting point. We describe our own studies of melting later.

The simplest assumption we can make about the potential is that it is pair additive. However, it is clear that this is only remotely valid for one family of atomic solids, namely the rare gas elements. The many-body contribution to the potential energy of these solids is very small for all normal (low-energy) structures, and their functional form and significance have been studied previously (1); we will not include them in this review. For all other atomic solids, it is well known that the pair-additive approximation fails badly, and there are five important properties that show this (2).

The first and simplest property is that of structure. Pair-additive potentials lead to the relative stabilization of highly coordinated close-packed structures. It is obvious that a structure such as diamond or graphite will not be favored by a simple pair potential, so such potentials cannot be applied to the covalently bonded solids of carbon, silicon, and many of the other *p*-block elements. However, as will be shown below, even for metals, where the close-packed (or nearly close-packed) structures are consistent with pair-additive forces, their dynamical and lattice dynamical properties are wrongly predicted by simple pair potentials.

The second property is known as the Cauchy equality. Cubic solids have three distinguishable elastic constants which are, by convention, labeled C_{11}, C_{12}, and C_{44}. A pair-additive ("central") potential leads to the result that $C_{12} = C_{44}$. As shown in Table 1, although the Cauchy equality holds well for rare gas solids (e.g., Ar and Kr) and some simple metals (such as the alkali metals and alkaline earth metals), most cubic metals have C_{12}/C_{44} ratios which are far from unity. In most cubic solids C_{12} is larger than C_{44}, but there are a few metals (such as Ir and Yb) for which

0022-4596/99 $30.00

TABLE 1
Indications of Many-Body Forces in Cubic Metals

Element	Structure	C_{12}/C_{44}	E_{vac}/E_{coh}
LJ	fcc	1.00	1.00
Ar	fcc	1.12	0.95
Kr	fcc	1.08	0.66
Li	bcc	1.12	0.21
Na	bcc	1.19	0.38
K	bcc	1.21	0.42
Ca	fcc	1.14	0.38
Sr	fcc	1.07	0.38
Al	fcc	2.29	0.19
Pb	fcc	2.47	0.25
Fe	bcc	1.15	0.47
Ir	fcc	0.95	0.26
Ni	fcc	1.26	0.36
Pt	fcc	3.28	0.26
Cu	fcc	1.61	0.33
Ag	fcc	2.03	0.36
Au	fcc	3.89	0.25
Yb	fcc	0.59	0.42

Note. Several fcc and bcc metals are compared with the fcc Lennard–Jones (LJ) solid (where the interatomic forces are pair additive) and the fcc rare gas solids Ar and Kr. (Adapted from Ercolessi *et al.* [2].)

this is not so and which are said to exhibit a negative Cauchy pressure, i.e., $C_{12} - C_{44} < 0$.

A third property of pair potentials is that they predict the energy of formation of an unrelaxed vacancy (E_{vac}) to be identical to the cohesive energy of the solid (E_{coh}). As shown in Table 1, although experimental vacancy formation energies for rare gas solids are similar to their cohesive energies, for metals E_{vac} is typically about one-third of E_{coh}. It should be noted that experimental vacancy formation energies refer to relaxed vacancies, but calculations indicate that relaxation energies are generally small (less than 15% of the unrelaxed vacancy formation energy) for metallic elements. Interestingly, while the Cauchy equality is approximately true for the alkali metals (e.g., Li, Na, and K) and alkaline earth metals (e.g., Ca and Sr), the ratio E_{vac}/E_{coh} is much less than unity, which shows that many-body forces are important even for these simple metals. This leads to the conclusion that although the existence of a significant Cauchy pressure (whether positive or negative) indicates the importance of many-body forces for a given elemental solid, the absence (or small magnitude) of a Cauchy pressure does not necessarily mean that many-body forces are insignificant.

The fourth property of pair-additive potentials is that when applied to unreconstructed surface structures (formed by taking a slice through the bulk) they predict that the spacing between the first (topmost) and second layer is always expanded relative to the bulk. The experimental fact, deduced from diffraction studies, is that the spacing of the most open surface generally contracts.

Finally, if a pair potential which reproduces the cohesive energy of the solid is chosen, then computer simulation of the melting process, using this potential, leads to a melting temperature in excess of that observed; a factor of 1.5–2.0 is typical.

We will add a sixth property that arises from our own studies: if the pair potential is assumed to have a simple functional form of the type well known for diatomic molecules, with a single turning point at the diatomic equilibrium distance, then no parameters can be found for this potential to give a good fit to the phonon dispersion curves. Pair potentials have been derived with several turning points (Friedel oscillations) which can fit the phonon curves but these are defined as volume-dependent potentials and they cannot be used for studies of phase transformations, surfaces, microclusters, etc., where large-density inhomogenieties are present (3). We see no grounds for encouraging further use of such potentials at the present time.

Moving beyond pair-additive potentials, there are two obvious lines of development, both of which have been studied extensively. The first is to adopt a many-body expansion and hope that this can be terminated at low order; in practice there have been few studies beyond three-body.

The second approach is to derive a potential for interatomic interactions which takes into account the totality of the neighbors of a given atom, as in the embedded atom model (EAM) and other so-called "glue potentials" (4). For practical use, such potentials are generally expressed in the form of a pair potential plus a functional of the positions of the neighboring atoms. Usually the functional is restricted to the first one or two shells of neighbors, depending only on their number and distance from the embedded atom. Embedded potentials of this kind contain no angle-specific terms and this is thought to be a weakness when modeling transition metals.

In this review, we summarize the results of our own particular approach to the development of potentials for atomic solids, in which we derive two-body and three-body terms by fitting experimental data. We aim to show that the reproduction of data is very good; that the potentials can be derived for all atomic solids which have a cubic structure (they could equally well be applied to noncubic structures, though the fitting procedure would be more complex), nonmetals, main group, transition and *f*-block metals, and that the potentials can easily be applied to structural and dynamic problems of atomic systems, without unreasonable demands on computer time. We will make comparisons with other potentials where appropriate and we will show that, in its generality and success, our approach performs extremely well compared with other models that have been investigated, within either an explicit or an implicit (embedded atom) many-body potential.

2. EMPIRICAL FITTING OF THE POTENTIAL TO EXPERIMENTAL DATA

In this section, we describe the data which are fitted in the empirical parameterization of our potentials and the importance that we attach to the various types of experimental observable.

First, we take the lattice energy (bulk cohesive energy, E_{coh}) and lattice constant (r_ℓ) of the cubic solid and use them to define energy and distance scaling factors, which reproduce these quantities exactly. Our fitting procedure cannot (in its present form) be applied to noncubic structures because they have more than one lattice constant, although the potentials may subsequently be used to explore such lower symmetry structures. Indeed, it is essential that the potential should give the correct ordering of lattice energies for a wide variety of cubic and noncubic phases.

Central to (and dominant in) our fitting procedure are the phonon dispersion curves. These are the vibration frequencies of the solid, expressed in reciprocal space as a function of the wave vector **q**. These curves are deduced from the results of inelastic neutron scattering experiments. In our fitting procedure, we select a number of points from the various phonon branches (curves) along the high-symmetry directions in the Brillouin zone: $(q, 0, 0)$; $(q, q, 0)$; and (q, q, q). Our reason for placing such high emphasis on phonon frequencies is that they explore, albeit for small displacements, the potential in all its multidimensionality. We make here an analogy with molecular potentials: our most extensive knowledge of molecular potential energy curves comes from the analysis of vibration frequencies, and it has been shown that, combined with equilibrium distances and dissociation energies, globally valid potentials can be produced for small molecules (5).

Following the theory of Born and von Kármán, the phonon dispersion curves can be expressed in terms of a set of harmonic force constants between an atom and its neighbors in the lattice. However, direct least squares fitting of these force constants independently of the phonon frequencies is not generally a satisfactory procedure because, by the time one has taken a sufficient number of force constants (i.e., summed out sufficiently far into the lattice) to get a good fit to the data, one has a multiplicity of sets of force constants from which to choose (6). Moreover, it is unlikely that any such phenomenological fitting, which is satisfactory (from a least squares fitting view point), extends sufficiently far into the lattice to include all non-negligible force constants.

Our fitting procedure is different from the above in that we have a potential which contains a limited number of parameters; from this the harmonic force constants can be calculated as far out into the lattice as we wish, without increasing the number of parameters, and a least squares fit to the phonon curves can be performed. The number of parameters is far less than the number of force constants that appear in the expressions for the phonon frequencies. In our procedure the force constants are not, therefore, an independent set.

To provide data for our least squares fitting procedure phonon frequencies are squared, multiplied by the mass of the atom, and divided by the lattice constant. This gives quantities which are linear in the harmonic force constants and which have the same dimensions (those of pressure) as the elastic constants. The three independent elastic constants of the cubic solid (C_{11}, C_{12}, and C_{44}) are also included in the fitting data. The elastic constants are related to the slopes of the phonon curves at zero wave vector and are often obtained from these when direct measurements are not possible, due to crystals being too small. We usually find that our potential gives a good least squares fit to both phonon and elastic constant data, but if this is not so, it is likely that one of the sets of data is in error. Our analysis shows that elastic constants are more sensitive to force constants between distant atoms in the lattice than are phonon frequencies.

The vacancy formation energy is a key quantity to be fitted in our method because together with the cohesive energy it gives us separate measures of the total two-body and total three-body contributions to the potential for the equilibrium lattice; this point will be elaborated upon in Section 3.

Experimental vacancy formation energies can be obtained from two types of experiment. One is a comparison of the temperature dependence of the lattice constant with the temperature dependence of the density, the latter of which is influenced by the formation of vacancies. It is assumed in this type of analysis that the number of vacancies is governed by a Boltzmann factor. A second method involves measurement of positron lifetimes in the lattice, as these have been found to correlate with the amount of free space in the lattice.

The experimental vacancy formation energy includes the relaxation of the atoms surrounding the vacancy and is therefore smaller than the unrelaxed vacancy formation energy (E_{vac}) which we use in our fitting procedure. We normally find, from our potentials, that the relaxation energy is small (less than 15% of E_{vac}), and we can ignore it. Alternatively, if we derive a potential assuming the relaxation energy is zero, then this potential can be used to calculate the relaxation and a correction made to the input data; a single iteration of this kind will be sufficient, given the accuracy to which such data are known.

Our standard computer program fits the parameters of the potential to the data described above using a least squares procedure based on minimizing the dimensionless quantity

$$fsq = \sum_i \left(\frac{P_i^{\text{obs}} - P_i^{\text{calc}}}{P_i^{\text{obs}}} \right)^2 w_i. \qquad [1]$$

P_i is the value of the ith datum point and w_i is the weight attached to this point. We normally define all weights as being equal (all $w_i = 1$) but this constraint can be relaxed in situations where some of the data are of poor accuracy or of suspect validity.

All potentials which we adopt must satisfy certain criteria, apart from having a low (usually the lowest) value for *fsq*. These criteria are important because we normally find that there is a range of potentials, with similar *fsq* values, for which other key quantities (not used in the fitting) may be different.

The most important criterion is that no other structure can be found which has a lower energy than the one for which the potential has been derived (assuming that this was known to be the most stable structure). To this end we routinely calculate the energies and lattice constants of the following: cubic solids—diamond, simple cubic (sc), body-centered cubic (bcc), and face-centered cubic (fcc); hexagonal solids—hexagonal close packed (hcp) and simple hexagonal (sh); and a number of 1-D chains (linear and zigzag) and 2-D nets and slabs. The slabs are double layers which correspond to the low-index surfaces ((100), (110), and (111)) of the fcc lattice. If, for example, we were deriving a potential from data for an fcc solid then we would reject any potential which predicts that the bcc structure (say) is more stable than fcc. We do, however, tolerate a slight preference of hcp over fcc (by no more than 0.001 eV) because we cannot rely on the functional form of our potential to reproduce the small energy differences that are generally found between the fcc and hcp structures.

When calculating structural energies we determine the cohesive energy as a function of the nearest-neighbor separation, while maintaining the symmetry of the structure, and find the minimum of the potential energy curve. We therefore also have an easy check that our potentials, with low values of *fsq*, do not give potential energy curves exhibiting unphysical behavior; we would normally only accept a potential that gives a smooth curve with a single minimum for each structure.

The above structural criteria are computationally very quick to impose and can be applied to any potential with a reasonably low *fsq* value. Any potential which passes this test is then examined further with respect to its predictions for surface energies and reconstructions. We can easily calculate the energies (E_{surf}) of the unrelaxed (100), (110), and (111) surfaces. The ratio of the (110) and (111) surface energies is particularly relevant to the so-called (1×2)-missing row reconstruction of the (110) surface; this reconstruction occurs only for a few fcc metals (Au and Pt for example) and we find, as do others, that it is only when the ratio $E_{\text{surf}}(111)/E_{\text{surf}}(110)$ is less than $\sqrt{2/3}$ that reconstruction occurs (7).

Calculation of the relaxed surface structures is a little more time consuming but is routinely done for all published potentials. Several layers of each surface are relaxed and there are usually some experimental data available pertaining to the top three or four layers. The common finding that the top interlayer spacing of the most open surface contracts, compared to the bulk is an important feature of our potential.

3. THE MURRELL–MOTTRAM MANY-BODY POTENTIAL

The Murrell–Mottram (MM) potential is expressed as a sum of two-body and three-body terms. Within this framework, the total potential for the lattice is given by

$$V_{\text{tot}} = \sum_i \sum_{j>i} V_{ij}^{(2)} + \sum_i \sum_{j>i} \sum_{k>j} V_{ijk}^{(3)} \qquad [2]$$

or

$$V_{\text{tot}} = \frac{1}{2} \sum_i \sum_{j \neq i} V_{ij}^{(2)} + \frac{1}{6} \sum_i \sum_{j \neq i} \sum_{k \neq i,j} V_{ijk}^{(3)}. \qquad [3]$$

In any solid, in which all atoms are equivalent, the potential energy can be expanded about any arbitrary atom (say atom 1) and the cohesive energy (a positive quantity) is obtained as

$$E_{\text{coh}} = -\frac{V_{\text{tot}}}{N} = -\left(\frac{1}{2} \sum_{j \neq 1} V_{1j}^{(2)} + \frac{1}{6} \sum_{j \neq 1} \sum_{k \neq 1,j} V_{1jk}^{(3)}\right), \qquad [4]$$

where N is the number of atoms summed over to obtain the total potential energy, V_{tot}. The above equation may be rewritten:

$$E_{\text{coh}} = -\left(\frac{1}{2} \sum_{j \neq 1} V_{1j}^{(2)} + \frac{1}{3} \sum_{j \neq 1} \sum_{k>j} V_{1jk}^{(3)}\right). \qquad [5]$$

The unrelaxed vacancy formation energy, defined as the energy required to remove an atom from a given bulk site and then to place it on the surface of the material—at a position remote from the original site, is given by

$$E_{\text{vac}} = -\left(\sum_{j \neq 1} V_{1j}^{(2)} + \sum_{j \neq 1} \sum_{k>j} V_{1jk}^{(3)}\right) - E_{\text{coh}} \qquad [6]$$

$$= -\left(\frac{1}{2} \sum_{j \neq 1} V_{1j}^{(2)} + \frac{2}{3} \sum_{j \neq 1} \sum_{k>j} V_{1jk}^{(3)}\right). \qquad [7]$$

Hence the total two-body contribution to the potential can be measured by

$$V_{\text{tot}}^{(2)} = 2(E_{\text{vac}} - 2E_{\text{coh}}) \qquad [8]$$

and the three-body contribution by

$$V_{\text{tot}}^{(3)} = 3(E_{\text{coh}} - E_{\text{vac}}). \quad [9]$$

Our only *a priori* constraints on the two-body potential are that it should be broadly typical of the diatomic potentials of stable diatomic molecules and that it should have few parameters. The flexibility of our potential—its ability to reproduce a set of input data—is primarily determined by parameters in the three-body term. The two-body function that we have chosen is the Rydberg function, which has been used for simple diatomic potentials. In units of reduced distance and energy, it has the form

$$\frac{V_{ij}^{(2)}}{D} = -(1 + a_2\rho_{ij})e^{-a_2\rho_{ij}}, \quad [10]$$

where

$$\rho_{ij} = \frac{r_{ij} - r_e}{r_e}. \quad [11]$$

This potential has a minimum, of depth D (the diatomic dissociation energy), at $\rho_{ij} = 0$ (i.e., $r_{ij} = r_e$, the diatomic equilibrium distance). The only parameter involved in our optimization process is a_2, which determines the range of the potential and is related to the curvature (force constant) of the potential at its minimum; D and r_e are determined by scaling to the experimental cohesive energy and lattice constant, respectively.

The most important criterion which is applied to the three-body term is that it is symmetric to permutation of the three atoms (i, j, k) defining each triangle. There are many ways to establish this, but the most elegant is *via* the use of combinations of interatomic coordinates (Q_1, Q_2, and Q_3) which are irreducible representations of the S_3 permutation group (isomorphic with the C_{3v} or D_3 point groups). For a given triangle (i, j, k) the Q_i coordinates are defined by:

$$\begin{pmatrix} Q_1 \\ Q_2 \\ Q_3 \end{pmatrix} = \begin{pmatrix} \sqrt{1/3} & \sqrt{1/3} & \sqrt{1/3} \\ 0 & \sqrt{1/2} & -\sqrt{1/2} \\ \sqrt{2/3} & -\sqrt{1/6} & -\sqrt{1/6} \end{pmatrix} \begin{pmatrix} \rho_{ij} \\ \rho_{jk} \\ \rho_{ki} \end{pmatrix}, \quad [12]$$

where

$$\rho_{\alpha\beta} = \frac{r_{\alpha\beta} - r_e}{r_e}. \quad [13]$$

$r_{\alpha\beta}$ represents one of the three triangle edges (r_{ij}, r_{jk}, and r_{ki}) and the labels Q_1, Q_2, and Q_3 implicitly stand for $Q_1(i, j, k)$, etc. It can be shown that all totally symmetric polynomials in $\rho_{\alpha\beta}$ can be expressed as sums of products of the so-called integrity basis (5)

$$Q_1, \quad Q_2^2 + Q_3^2, \quad Q_3^3 - 3Q_3Q_2^2, \quad [14]$$

where Q_1 is the perimeter of triangle (i, j, k), in reduced coordinates, and the other two terms measure distortions away from an equilateral geometry.

If we take, for example, a general cubic term in a polynomial, then to make this totally symmetric with respect to interchange of atom labeling we could write this in $\rho_{\alpha\beta}$ coordinates as

$$a_1(\rho_{ij}^3 + \rho_{jk}^3 + \rho_{ki}^3) + a_2(\rho_{ij}(\rho_{jk}^2 + \rho_{ki}^2) + \rho_{jk}(\rho_{ij}^2 + \rho_{ki}^2) + \rho_{ki}(\rho_{ij}^2 + \rho_{jk}^2)) + a_3(\rho_{ij}\rho_{jk}\rho_{ki}). \quad [15]$$

Alternatively, in Q-coordinates we have

$$b_1Q_1^3 + b_2Q_1(Q_2^2 + Q_3^2) + b_3(Q_3^3 - 3Q_3Q_2^2). \quad [16]$$

A further condition to be imposed on $V_{ijk}^{(3)}$ is that it should go to zero as any one of the three atoms goes to infinity. In keeping with the functional form adopted for the two-body potential, we have adopted a general family of three-body functions

$$\frac{V_{ijk}^{(3)}}{D} = P(Q_1, Q_2, Q_3)F(a_3, Q_1), \quad [17]$$

where P is a polynomial in the Q-coordinates and F is a damping function which decays exponentially at long range (high values of the triangle perimeter Q_1). F contains a single parameter, a_3, an exponent which determines the range of the three-body potential. We have used three types of damping functions in our work, namely

$$\begin{aligned} F(a_3, Q_1) &= \exp(-a_3Q_1) && \text{exponential} \\ F(a_3, Q_1) &= \tfrac{1}{2}(1 - \tanh(a_3Q_1/2)) && \tanh \\ F(a_3, Q_1) &= \operatorname{sech}(a_3Q_1) && \text{sech.} \end{aligned} \quad [18]$$

Most of the early work with the MM potential was carried out with the exponential damping function, but one problem that emerged was that for large negative Q_1 values (i.e., for triangles for which $r_{ij} + r_{jk} + r_{ki} \ll 3r_e$) the function F may be large and give an overall three-body contribution (after summing over all triangles) to the potential which swamps the total two-body potential. If the polynomial P is negative for these small triangles the three-body potential may become large and negative, and may lead to the collapse of the lattice. (Note that although the Rydberg function is positive—repulsive—for $r \ll r_e$, it does not go to

infinity as r approaches zero.) To overcome this problem requires us, in some cases, to introduce an additional "hard wall" to the repulsive side of the two-body term. While we continue to keep this as an option, it is rarely necessary when using the tanh function (which goes to the limiting value of 1 as Q_1 tends to minus infinity). Even less trouble is encountered using the sech function, which tends to zero for large negative Q_1 values. Both the tanh and sech functions decay as $e^{-a_3 Q_1}$ for large Q_1 values. Our favored choice in recent work has been the sech function, but all three are usually examined for each element studied.

The polynomial P is normally taken as far as the cubic level and written

$$P(Q_1, Q_2, Q_3) = c_0 + c_1 Q_1 + c_2 Q_1^2 + c_3(Q_2^2 + Q_3^2) + c_4 Q_1^3 + c_5 Q_1(Q_2^2 + Q_3^2) + c_6(Q_3^3 - 3Q_3 Q_2^2), \quad [19]$$

so there are seven coefficients to be determined. If the data warrant it (e.g., in some cases where simultaneous fitting is made to data for two different solid phases) we add the quartic terms

$$c_7 Q_1^4 + c_8 Q_1^2(Q_2^2 + Q_3^2) + c_9(Q_2^2 + Q_3^2)^2 + c_{10} Q_1(Q_3^3 - 3Q_3 Q_2^2). \quad [20]$$

There is another useful feature of the Q-coordinates that should be noted here. If we have *ab initio* data on the energy of a three-atom structure only for C_{2v} geometries (isosceles triangles for which $Q_2 = 0$) then these are sufficient to allow the unambiguous determination of coefficients in a polynomial up to fifth order in Q_i, because it is only at sixth order that we have an ambiguity between $(Q_2^2 + Q_3^2)^3$ and $(Q_3^3 - 3Q_3 Q_2^2)^2$ that can only be resolved using data on scalene triangles.

4. COMPUTER PROGRAMS

Our work, using the Murrell–Mottram potential has been accomplished using a suite of five FORTRAN computer programs. A brief description of the functions of these programs is presented here.

1. CUBEPRO optimizes the potential (i.e., determines the optimum set of exponents and polynomial coefficients) by fitting specified input data, described in Section 2, for fcc or bcc solids. The program can also be used to fit a potential simultaneously to data sets from two allotropes (fcc and bcc), as has been done for Fe, Ca, and Sr.

2. SOLIDS calculates the nearest-neighbor distances and cohesive energies of a number of one-, two-, and three-dimensional structures, using the potential output from CUBEPRO. This program is used to check that the potential gives sensible ordering of the cohesive energies for different structures and sensible shapes for their potential energy curves.

3. SURFPRO calculates the structures and energies of relaxed surfaces (fcc and bcc) and checks for missing row reconstruction of the fcc (110) surface. The unrelaxed surface energies are calculated first, and these may be fed into CUBEPRO and used in the potential optimization process, though this option is rarely used.

4. CLUSPRO takes potentials generated by CUBEPRO and calculates energies of microclusters. Small clusters (typically up to 50 atoms) are constructed as fragments of bulk solids or are generated randomly. Their geometries are optimized by quasi-Newton or conjugate gradient energy minimization, and Monte Carlo or molecular dynamics simulated annealing. Larger clusters (with up to several hundreds or thousands of atoms) are generated as concentric polyhedral shells of atoms, which are optimized by minimizing their energy as a function of the radii of the individual shells and subshells (sets of symmetry equivalent atoms).

5. MELTPRO takes potentials derived by CUBEPRO and uses a Monte Carlo algorithm to examine the melting of bulk solids and surfaces, by monitoring the variation of certain structural order parameters as a function of temperature.

The only one of these programs which will now be described in more detail is CUBEPRO, because its special features are directly relevant to the functional form of the potential we have chosen.

The program optimizes the set of polynomial coefficients $\{c_i\}$ to the input data specified earlier, for selected values of the exponents a_2 and a_3, a search being made over the (a_2, a_3) grid. This procedure is more efficient than the alternative, in which a_2 and a_3 are included in the set of parameters to be optimized by the program, because the *fsq* surface is much flatter in exponent (a_2, a_3) space than it is in coefficient $\{c_i\}$ space. In only a few cases do we find that changes in a_2 and a_3 of less than ± 0.5 give any marked difference in the quality of fit, whereas changes in $\{c_i\}$ of as little as 10^{-2} have a noticeable effect on *fsq*. We normally, therefore, determine *fsq* on an integer grid of (a_2, a_3)—both exponents normally lying between 5 and 10—and select the potentials from regions of low *fsq* for further examination.

The method for finding an optimum set of coefficients (for fixed a_2 and a_3) is as follows:

(i) An initial set of coefficients $\{c_i\}$ is chosen (normally all zero or values taken from a previous optimization, e.g., from the preceding point on the (a_2, a_3) surface). The potential energy (in reduced units) is calculated for an initial large nearest-neighbor separation ($\rho = 2r_e$, say) and the potential energy minimum (i.e., the cohesive energy maximum) is found by performing a line search minimization, with ρ decreasing in steps of 0.001 and a final three-point parabolic fitting to find the minimum. This gives an equilibrium

nearest-neighbor distance ρ_e and minimum potential energy (in reduced units) V_{min}. Comparison with the experimental nearest-neighbor distance (r_{nn}) and bulk cohesive energy (E_{coh}) of the reference structure enable the scaling distance (r_e) and energy (D) to be obtained as

$$r_e = \frac{r_{nn}}{\rho_e} \quad [21]$$

and

$$D = -\frac{E_{coh}}{V_{min}}, \quad [22]$$

(ii) We now have an initial potential, from which harmonic force constants can be calculated, and, following the lattice dynamical method of Born and von Kármán, phonon frequencies and elastic constants can be calculated. The squared differences between the experimental and calculated phonon data (as specified earlier) and elastic constants are then summed to give *fsq*. We also add in the errors in the vacancy energy and any other property (surface energy etc.) that is specified.

(iii) A NAG (8) routine (e04fcf) is used to perform a least squares minimization of *fsq* as a function of the polynomial coefficients $\{c_i\}$. This is based on making initial very small changes in $\{c_i\}$ and determining the slopes $\partial(fsq)/\partial c_i$ and curvatures $\partial^2(fsq)/\partial c_i \partial c_j$ numerically. The program typically performs on the order of 100 iterations of *fsq* in optimizing the coefficients of a cubic polynomial to a level at which *fsq* changes by less than 0.001 between successive iterations.

A run of approximately 2.5 h for a 10-shell potential or 1 h for a 5-shell potential (on an IBM RS6000 computer) can produce integer (a_2, a_3) grids (with exponents in the range 5–10) for the three damping functions defined above. The behavior of the low *fsq* potentials can then be checked using the program SOLIDS, in order to remove any that are unsuitable. However, we stress that acceptable potentials are always found in the region of low *fsq*'s; we do not accept potentials from high *fsq* regions, even if they behave well according to other criteria.

Finally, we note that a single program can handle fcc and bcc solids (and simple cubic, if data were available). However, because the unit cell of the diamond structure has two (rather than one) atoms in the primitive unit cell, the lattice dynamics of diamond are more complex than for the other three (monatomic) cubic solids. For this reason, a separate program, DIPRO, has been written to generate potentials for diamond solids (e.g. C, Si, Ge, and Sn) though its basic structure is identical to that of CUBEPRO.

5. OPTIMIZED MM POTENTIALS

Many-body MM potentials have been derived for over 20 main group, transition metal and lanthanide elements whose room temperature crystal structures have cubic symmetry. The MM potentials are listed in Table 2 (cubic three-body polynomials) and Table 3 (quartic three-body polynomials). In those cases where more than one potential has been obtained for the same element, only the most recent is reproduced. Other potentials can be found in the original papers cited in this review. Some examples, chosen to illustrate our methodology, are discussed below.

5.1. Single Phase Optimization

5.1.1. Potentials for the group 14 elements. The first MM potentials developed were cubic potentials for the group 14

TABLE 2
Optimized Cubic MM Potentials with a Cutoff of $3\times r_{nn}$ (i.e., 11 Shells for bcc and 10 shells for fcc)

	Ref.	a_2	a_3	F^a	D (eV)	r_e (Å)	c_0	c_1	c_2	c_3	c_4	c_5	c_6
Li	(28)	6.5	6.5	e	0.4194	3.1399	0.1818	1.1328	2.2128	− 2.4618	− 1.0149	− 0.4999	1.9815
Na	(28)	7	7	e	0.2632	3.7511	0.1805	1.1755	1.8303	− 2.9624	− 2.7386	1.3416	2.9384
K	(28)	7	7	e	0.2218	4.6543	0.1744	1.1154	1.8805	− 2.8751	− 1.8022	0.6185	2.8787
Rb	(28)	7.5	7.5	e	0.2157	4.9789	0.2084	1.3831	2.7395	− 3.7531	− 2.4645	− 0.3562	3.8054
Cs	(28)	7.5	8.0	e	0.2154	5.3505	0.2306	1.6112	4.4354	− 4.0538	− 3.1694	− 1.5639	3.5544
Ni	(74)	8.5	10	s	1.189	2.394	0.226	− 0.018	5.334	− 2.856	− 1.294	− 0.380	2.381
Pd*	(33)	7	10.2	s	0.946	2.667	0.197	− 0.221	6.516	− 0.435	10.273	− 14.543	4.463
Pt*	(33)	8.5	9	s	1.613	2.699	0.244	− 0.429	5.814	− 2.581	1.268	− 7.386	5.401
Cu	(26)	7	9	s	0.888	2.448	0.202	− 0.111	4.990	− 1.369	0.469	− 2.630	1.202
Ag	(26)	7	9	s	0.722	2.799	0.204	− 0.258	6.027	− 1.262	− 0.442	− 5.127	2.341
Au	(26)	9	10	s	1.100	2.785	0.284	− 0.385	7.086	− 2.799	2.859	− 11.273	6.215
Al*	(45)	7	8	s	0.9073	2.7568	0.2525	− 0.4671	4.4903	− 1.1717	1.6498	− 5.3579	1.6327
Yb	(75)	6	8	e	0.300	4.127	0.128	1.306	2.953	− 1.010	− 0.483	− 2.841	1.090

Note. * Potentials were optimized with a cutoff of $2.25\times r_{nn}$ (5 fcc shells).
[a] Type of decay function: e, exponential; s, sech.

TABLE 3
Optimized Quartic MM Potentials with a Cutoff of $3\times r_{nn}$ (i.e., 11 Shells for bcc and 10 shells for fcc)

	Ref.	a_2	a_3	F^a	D (eV)	r_e (Å)	c_0 c_7	c_1 c_8	c_2 c_9	c_3 c_{10}	c_4	c_5	c_6
Ca†	(25)	6.0	11.5	t	0.3799	3.9372	0.1174 56.6397	1.7882 13.9832	10.1597 −27.2587	1.1767 33.6836	12.7462	−16.7545	7.9449
Sr†	(25)	6.0	11.0	s	0.3353	4.4714	0.0873 24.7129	0.1219 −35.0423	2.6310 −2.4595	−0.3362 7.9207	21.2253	3.0820	0.0446
Fe†	(22)	6.55	9.6	e	0.8847	2.6832	0.1760 13.2511	1.7958 −8.3421	5.0885 4.5088	−2.9047 −0.5670	−2.2007	−6.1349	2.8605
C*	(17)	8.2	8.2	e	6.298	1.507	8.087 −5.964	−13.334 −7.306	26.882 2.208	−51.646 13.707	12.164	51.629	25.697
Si*	(16)	6.5	6.5	e	2.918	2.389	3.598 23.383	−11.609 −111.809	13.486 9.705	−18.174 38.297	−5.570	79.210	−6.458
Ge*	(16)	6.5	6.5	e	2.330	2.559	2.986 33.565	−13.778 −99.248	29.843 8.881	−14.291 30.103	−28.628	61.935	−1.418
Sn*	(16)	6.25	3.55	e	1.000	2.805	1.579 2.949	−0.872 −15.065	−4.980 10.572	−13.145 12.830	−4.781	35.015	−1.505

Note. *diamond potentials were optimized with a cutoff of $2.6\times r_{nn}$ (5 shells); †Elements have dual-optimized potentials (i.e., fitted to more than one solid phase).

[a]Type of decay function: e, exponential; s, sech; t, tanh.

elements C, Si, and Ge (9, 10). These potentials were fitted to a limited set of data for the diamond allotropes of each element. In all cases, the diamond (dia) structure was found (using the program SOLIDS) to be the most stable cubic structure, with the cohesive energies (E_{coh}) varying as dia > sc > bcc > fcc, in agreement with experiment and with other empirical potentials (e.g., the Stillinger–Weber (11), Tersoff (12), and Biswas–Hamann (13) potentials) and the density functional calculations of Yin and Cohen (14, 15). In the case of carbon, the graphite structure was (correctly) predicted to be more stable than diamond, though the difference was overestimated.

Improved quartic potentials for C, Si, Ge, and Sn were obtained by including the energies and lattice spacings of other allotropes in the fitting (16, 17). For Si and Ge, calculated values for the lattice energies and lattice spacings of the sc, bcc, and fcc structures were used (14), while experimental data were used for C (graphite) and the tetragonal (β) allotrope of Sn. The best carbon potential gives a graphite interlayer separation of 3.21 Å and an interlayer interaction energy of 0.001 eV per atom (17). The quartic potentials listed in Table 3 are taken from Ref. (17) (for C) and Ref. (16) (for Si, Ge, and Sn).

As shown in Fig. 1, the calculated phonon dispersion curves for Si agree qualitatively with experimental values, although the agreement at the Brillouin zone edge is not very good. A more extensive investigation of Si potentials was subsequently performed which produced a significant improvement in the quality of the fit to the phonon dispersion curves (18). We have recently investigated the extension of the MM potential by adding four-body terms, and we have found that the addition of such terms can lead to an extra, small improvement in the fit to experimental data for silicon (18). The general applicability and cost-effectiveness (in terms of extra computational time required for a given improvement in fit) of four-body potentials are currently being studied.

5.1.2. Potentials for the alkali metals. Though the MM potential was initially formulated to study covalent solids, such as the group 14 elements, it has proved very successful for modeling the structures and dynamics of metallic elements. For example, cubic MM potentials were derived for the alkali metals Li–Cs by fitting phonon frequencies, elastic constants, lattice energies, and lattice spacings of the bcc metals. The quality of the fit between calculated and experimental phonon dispersion curves can be seen in Fig. 2, for the specific example of sodium. When tested with the program SOLIDS, these potentials all gave very similar energies for the bcc, fcc, and hcp structures, with the sc, diamond, and various 2-D structures being considerably less stable. There is experimental evidence that Li and Na

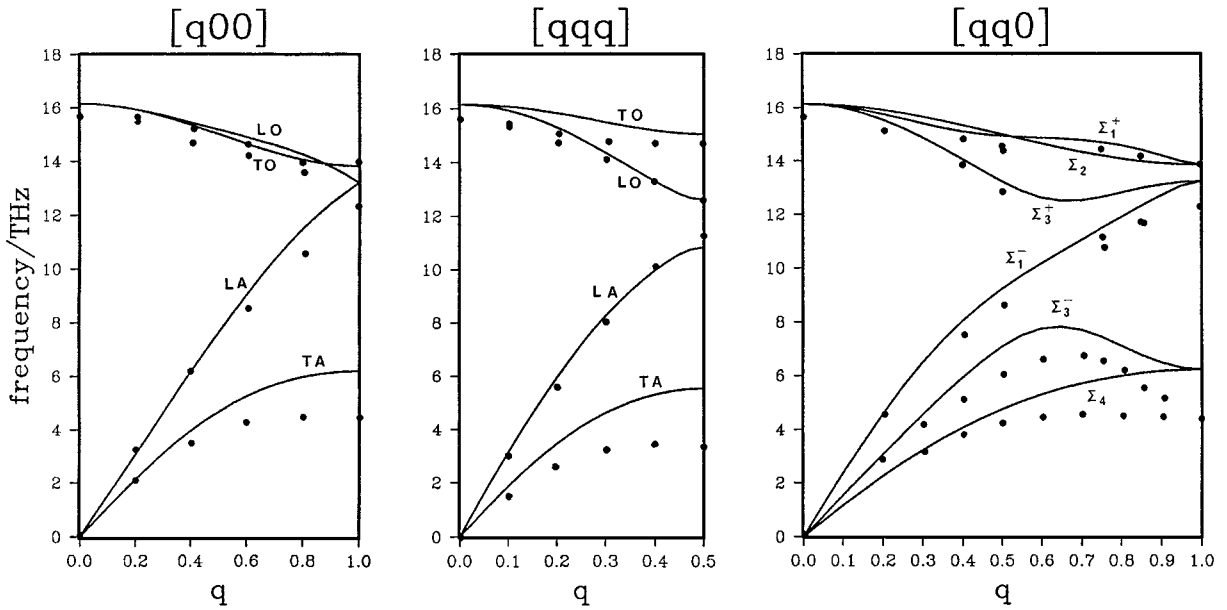

FIG. 1. Calculated phonon dispersion curves for silicon (diamond structure) along high-symmetry lines [q00], [qq0], and [qqq] in the Brillouin zone (10). Experimental frequencies are represented by points. The q's are given as fractions of $2\pi/r_\ell$.

have close-packed structures (fcc or hcp) at very low temperatures (19), and pseudopotential calculations for Na and Rb, by Maysenholder *et al.* (20), also make the bcc and fcc structures approximately degenerate.

5.2. Dual Optimization

Many elements are found to adopt more than one structure, depending on conditions of temperature and/or pressure (19) and, in a number of cases, lattice dynamical data (in particular phonon frequencies) are available for some of these structures. This affords us the possibility of simultaneously fitting a potential to the structures, energies, and lattice dynamics of more than one phase. So far, we have concentrated on dual optimization of potentials (i.e., fitting to two structures), with the aim of deriving "global" potentials which are applicable over a wide range of configuration and coordination space.

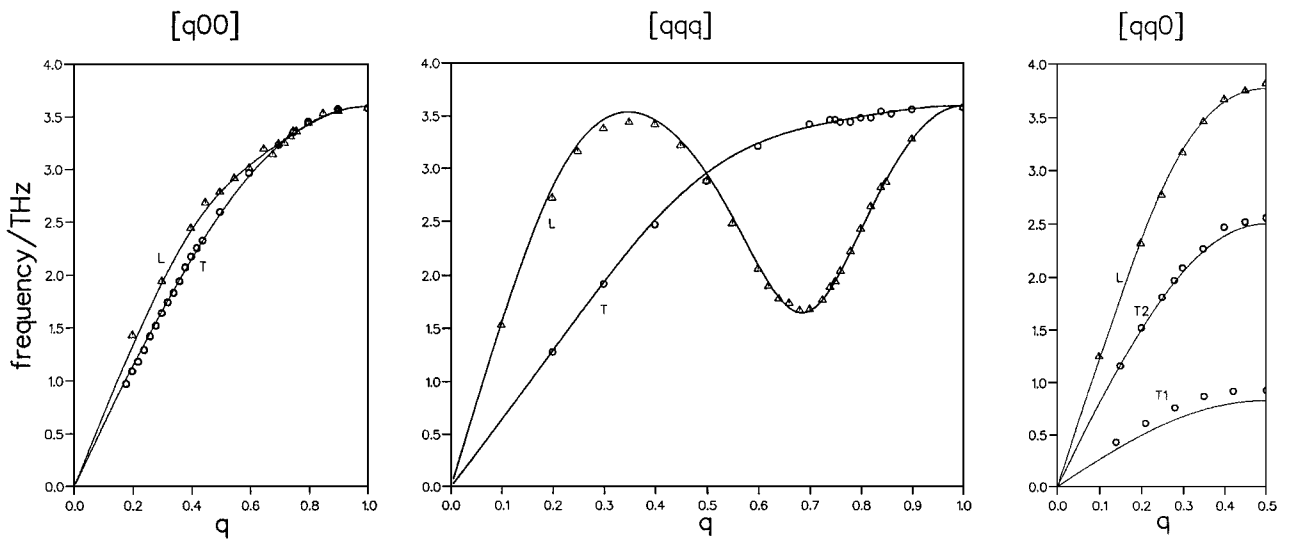

FIG. 2. Calculated phonon dispersion curves for bcc sodium along high-symmetry lines [q00], [qq0] and [qqq] in the Brillouin zone (28). Experimental frequencies are represented by circles and triangles. The q's are given as fractions of $2\pi/r_\ell$.

5.2.1. A dual-optimized potential for iron. The study of iron is of great interest, both experimentally and theoretically, due to its importance in materials science and geology. It exhibits many polymorphs so there is a clear need for a potential which is valid over a range of structures and which can be used to study the static and dynamic properties of solid and liquid iron as a function of temperature and pressure (21).

The normal (ambient temperature and pressure) phase of iron is α-Fe, which has the bcc structure and is ferromagnetic. At around 1200 K, iron undergoes a phase transition to the fcc form, γ-Fe, which is paramagnetic (i.e., there is no long-range spin ordering). Other phases can be prepared under appropriate conditions of temperature and pressure (19).

A quartic potential (listed in Table 3) was derived for iron by simultaneously fitting the phonon frequencies and elastic constants of both the α- and γ-forms of Fe (22). The vacancy formation energy of α-Fe was also included in the fitting. In the dual optimization approach, the lattice spacing and cohesive energy of the low-temperature structure (in this case bcc α-Fe) are fixed via the scaling parameters r_e and D, and the corresponding values for the high-temperature structure (in this case fcc γ-Fe) are allowed to vary. A cutoff of three times the nearest-neighbor distance (i.e., 11 shells for bcc and 10 shells for fcc) is generally adopted.

Using the dual-optimized potential, both the bcc and fcc phases were calculated to be mechanically stable (i.e., all phonon frequencies are real and $C_{11} > C_{12} > C_{44} > 0$) using the dual-optimized potential. The phonon dispersion curves for α- and γ-Fe are shown in Fig. 3, from which it can be seen that the fit between theory and experiment is very good. The calculated cohesive energy of fcc γ-Fe (4.26 eV) is slightly smaller than the (fixed) value for bcc α-Fe (4.28 eV), and the vacancy energy calculated for γ-Fe (1.79 eV) is also smaller than that for α-Fe (1.81 eV; note that the experimental value is 2.0 eV), which again is satisfactory. The lattice spacing calculated for γ-Fe is 3.73 Å, which compares well with the experimental value (extrapolated to 1428 K) of 3.68 Å. Finally, the Fe potential reproduces the stability order of other 1-, 2-, and 3-D phases found in previous DFT calculations by Paxton *et al.* (23) and by Baskes, using an alternative empirical potential (24).

This work on iron proved that it was possible to optimize potentials by fitting, simultaneously to two or more phases, and we have subsequently derived such global potentials for calcium and strontium (25).

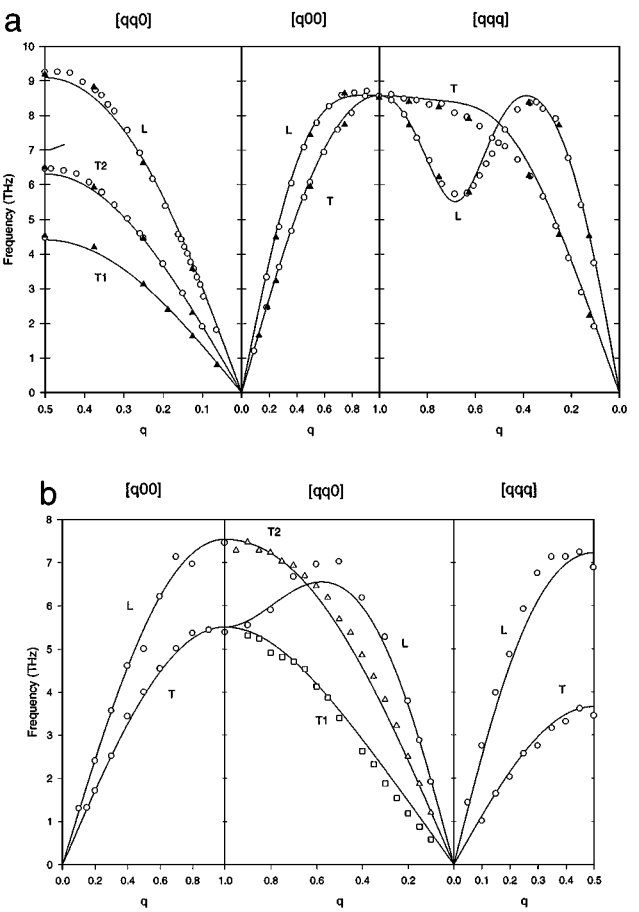

FIG. 3. Phonon dispersion curves calculated for (a) bcc α-Fe and (b) fcc γ-Fe along high-symmetry lines [q00], [qq0], and [qqq] in the Brillouin zone using the dual-optimized MM iron potential (22). Experimental frequencies are represented by circles and triangles. The q's are given as fractions of $2\pi/r_\ell$.

5.3. Force Constants

The Born–von Kármán harmonic force constants for the first four shells of fcc Au, calculated using the 10-shell MM cubic potential (26), are compared to those calculated by Lynn *et al.*, based on a 4-shell fit to their measured phonon dispersion curves (27), in Table 4. It is evident that, while there is good agreement for the first and second shell force constants, the agreement for the third and fourth shell force constants is poor. Differences are to be expected because our MM potential extends to 10 shells (i.e., a cutoff of $3 \times r_{nn}$) whereas the phenomenological force constants are taken to be zero beyond 4 shells. Also, our force constants are constrained (interrelated) by their being derived from a physical potential energy function, while the 12 force constants of Lynn *et al.* are freely optimized, but with no such physical restraint. Similar conclusions have been drawn when comparing MM and phenomenological force constants for other elements (22) and we see no reason for assuming that a sharply terminated set of phenomenological force constants should be any closer to the true values than our own which extend far into the lattice.

TABLE 4
Comparison of First to Fourth Shell Born–von Kármán Force Constants Calculated for fcc Au (Using the Cubic MM Potential (26)) with Those Fitted to the Experimental Phonon Frequencies by Lynn *et al.* (27)

Shell	Force constant	MM (26)	Ref. (27)
1	XX	1.675	1.643
	ZZ	−0.572	−0.654
	XY	1.932	1.993
2	XX	0.360	0.404
	YY	−0.118	−0.127
3	XX	0.027	0.080
	YY	−0.004	0.039
	XY	0.007	0.004
	YZ	0.009	0.016
4	XX	0.001	−0.075
	ZZ	0.001	−0.014
	XY	0.001	−0.036

Note. The force constants have units of 10^4 dyn cm^{-1}, and the symmetries of the force constant matrices have been described by Johnston and Fang (32).

5.4. Correlations between MM Potentials

It is interesting to compare qualitative features of and trends in the parameters of the MM potentials that have been derived (see Tables 2 and 3) for various groups of elements.

In considering first the cubic MM potentials for Li–Cs (see Table 2), it is clear that the potentials are qualitatively very similar, in that all of the polynomial coefficients have the same sign for all of the alkali metals, with the exception of c_5, which is positive for Na and K, and negative for Li, Rb, and Cs. The signs of the coefficients c_0–c_6 therefore exhibit the pattern $[+++--\mp+]$. The magnitudes of the coefficients are also very similar from element to element. Though the exponents a_2 and a_3 increase slightly on descending the group, the range of the potentials actually increases on going from Li to Cs, because the ratio a/r_e decreases (28). The similarities and simple trends in the potentials reflect similarities in the phonon dispersion curves and elastic constants (taking into account mass-dependent scaling) of these elements, which in turn reflect the similar bonding characteristics of the metals (all are bcc at ambient temperature and pressure).

The cubic MM potentials for the fcc noble metals Cu, Ag, and Au are also qualitatively very similar (26), again reflecting their similar phonon dispersion curves (29). The only qualitative difference occurs for c_4, which is positive for Cu and Au, but negative for Ag. The group 10 metals Ni, Pd, and Pt also adopt the fcc structure, and their cubic potentials are very similar to those of the noble metals. Again, the main difference occurs for c_4, which is negative for Ni but positive for Pd and Pt. The cubic potential for aluminum is qualitatively the same as for the other fcc metals. For Al, c_4 is positive (as for Cu, Au, Pd, and Pt). The pattern of the coefficients c_0–c_6 for fcc metals may therefore be written $[+-+-\pm-+]$.

Comparing the cubic potentials for the bcc alkali metals with the cubic fcc potentials, we see that the major difference is in c_1, which is positive for bcc metals but negative for fcc. Also, while c_4 is negative for the bcc metals, it is usually positive for fcc. Finally, while c_5 may be positive or negative for bcc metals, it appears always to be negative for fcc.

The cubic potential for Yb is unusual in that, although the ground state structure is fcc, the signs of the coefficients are the same as those of the bcc alkali metals Li, Rb, and Cs. This may be because Yb also has a low lying metastable bcc phase.

In turning to the quartic potentials listed in Table 3, the coefficients c_0–c_6 of the Fe potential (with a bcc ground state structure) adopt the same pattern ($[+++---+]$) as do most of the alkali metals (Li, Rb, and Cs) and Yb. There is, however, no such similarity between the quartic potentials of the (fcc) alkaline earth metals Ca and Sr, when compared either to each other or to the cubic fcc potentials listed in Table 2. This may be because they have been optimized to both fcc and bcc structures, but more likely reflects the fact that quartic potentials with large quartic coefficients (c_7–c_{10}) appear to exhibit little similarity, owing to the nonorthogonality of the terms in the polynomial.

In comparing the quartic MM potentials for the group 14 elements, listed in Table 3, it is apparent that there are a number of similarities between these elements, which is consistent with the fact that all four potentials were optimized by fitting properties of the diamond-structure allotropes. Particularly noteworthy is the very close similarity, in terms of both signs and magnitudes, of the coefficients of the Si and Ge potentials. This similarity is to be expected since the phonon dispersion curves and elastic constants of Si and Ge are so similar and can be approximately scaled onto each other by correcting for the different atomic masses. The Sn potential differs qualitatively from that of Si and Ge only in the sign of c_2, which is negative, rather than positive, although there are significant differences in the magnitudes of some of the coefficients. These differences are consistent with the different physical properties of Sn and the fact that the diamond structure is unstable with respect to the metallic β-Sn structure above 286 K (19). The carbon potential has a different coefficient pattern from that of the Si and Ge potentials, there being different signs for c_4, c_6, and c_7. There are also significant differences in the magnitudes of some of the coefficients. These differences are consistent with the fact that of the group 14 elements, only carbon has the graphite structure as the most stable allotrope.

Finally, it should be noted that the coefficients c_0–c_6 for C–Sn are qualitatively very different from those for the bcc or fcc metals (which are qualitatively quite similar to each other). This is not surprising, since one would expect that the three-body potential, which makes the "open" diamond structure more stable than more close-packed structures, should be quite different from potentials which stabilize the geometrically similar bcc and fcc structures (30).

6. STRUCTURES AND STABILITIES OF SOLID STRUCTURES

If a potential is to be used to study liquids, surfaces, clusters, etc., it must be applicable over a wide range of coordination numbers and geometries. As explained in Section (4) the stabilities and structures of a number of solid phases, in addition to those whose properties have been used in the derivation of the potential, are calculated by the program SOLIDS.

The structures we have considered are those compared by Robertson *et al.* in a study of Al solids using DFT calculations and empirical glue-type potentials (31). These structures are now routinely investigated for all elements for which MM potentials are derived (32).

The three-dimensional structures studied are fcc, bcc, sc, diamond, simple hexagonal (AAA stacking of triangular nets), and a concentrated vacancy structure which is generated by removing one-quarter of the atoms in the fcc lattice and which consists of a three-dimensional array of vertex-sharing octahedra. In addition, we also looked at the idealized hcp lattice (with the cell parameter $c_{\text{hex}} = \sqrt{8/3}a_{\text{hex}}$ so that, as in the fcc structure, the 12 nearest neighbors are all at the same distance.

The two-dimensional structures consist of single layers (triangular net, square net, hexagonal net [i.e., a single graphite layer]) and two-layer slabs (triangular slab [i.e., eclipsed triangular nets], square slab [eclipsed square nets], and three slabs ($f100$, $f110$, $f111$) corresponding to the top two layers of the fcc (100), (110), and (111) surfaces, respectively. Obtaining reasonable relative energies for these structures is of great importance if our potential is subsequently to reproduce the properties of surfaces accurately.

Finally the one-dimensional structures are the linear chain and the zigzag chain (31), which is essentially a ribbon of edge-sharing triangles.

6.1. Relative Stabilities of Aluminium Solids

All the potentials listed in Tables 2 and 3 give cohesive energies and interatomic distances which are consistent with available knowledge, and we illustrate this here for aluminum, for which we have the best independent data for comparison.

Table 5 shows the cohesive energies and equilibrium nearest-neighbor distances calculated for a variety of real and hypothetical one-, two-, and three-dimensional Al structures, using the program SOLIDS and the 5-shell cubic MM potential for Al (33) listed in Table 2. Table 5 also lists the coordination numbers (the number of nearest neighbors), number of shells, and total number of atoms out to a cutoff of $2.25 \times r_{\text{nn}}$ (corresponding to a 5-shell cutoff for the fcc structure). Also given are our calculated equilibrium nearest-neighbor distances (d_{nn}) and cohesive energies (U_{e}) as well as the cohesive energies (U_{f}) calculated at fixed nearest-neighbor separation ($d_{\text{nn}} = r_{\text{nn}}(\text{fcc}) = 2.84$ Å) so that comparison can be made with those (U_{R}) calculated by Robertson *et al.* at fixed separation (actually 2.85 Å) (31).

It is noticeable that there is a general increase in cohesive energy with increasing coordination number. As can be seen from Table 5, within each set of structures (3-D, 2-D slabs, 2-D nets, and 1-D chains) the stability ordering that we obtain is identical to that of the DFT calculations of Robertson *et al.* (31). In fact the numerical agreement is also good for the 3-D structures (with the exception of diamond, which we find to be significantly less stable). The relative stabilities of the various sets of structures are also well reproduced by our calculations, with the exception that we calculate the $f111$ slab to be less stable than the 3-D sc lattice.

Heine and co-workers showed that a simple glue model based on the coordination number alone gives a good fit to the *ab initio* DFT cohesive energies of a wide range of structures (4, 31, 34). Our many-body MM potential for Al is in good agreement with the DFT calculations and has been shown, moreover, to give an excellent fit to elastic constants, phonon frequencies, and surface energies (32, 33). The geometry-dependent nature of our potential, which comes in through the three-body term, results in correct relative energies (by comparison with the *ab initio* calculations) of structures with the same coordination number but differing local geometries.

6.2. The Bain Path for fcc–bcc Interconversion

Several elements adopt two or more solid state structures depending on temperature and pressure. The alkaline earth metals calcium and strontium, for example, adopt the fcc structure at ambient temperatures and pressures but transform to the bcc structure at high T or P (19). For these and some other elements we have investigated the tetragonal Bain deformation, which interconverts fcc and bcc via an intermediate body-centered tetragonal (bct) structure (35). Other diffusionless transformations can interconvert the fcc and bcc structures (36), but the Bain path is particularly interesting as it involves the minimum of atomic movement and, hence, the minimum strain in the lattice. Here, we present results for calcium (25).

TABLE 5
Nearest-Neighbor Separations and Cohesive Energies Calculated for Some One-, Two-, and Three-Dimensional Aluminum Structures, Using the Cubic MM Potential (45)

Structure	C.N.[a]	No. shells[b]	No. atoms[c]	r_{nn} (Å)[d]	U_e (eV)[e]	U_f (eV)[f]	U_R (eV)[g]
3-D							
fcc	12	5	78	2.84	3.39	3.39	3.36[h]
hcp	12	7	68	2.84	3.39	3.39	—
fcc vacancy	8	5	58	2.70	3.17	3.04	3.15
bcc	8	5	58	2.81	3.35	3.34	3.29
Simple hexagonal	8	5	70	2.70	3.28	3.13	3.17
sc	6	5	56	2.69	3.05	2.83	2.96
Diamond	4	3	28	2.63	2.16	1.94	2.47
2-D slabs							
*f*111	9	5	36	2.78	2.89	2.88	3.02
Triangular	9	5	37	2.71	2.82	2.72	2.94
*f*100	8	5	36	2.75	2.76	2.72	2.90
*f*110	6	5	22	2.71	2.40	2.33	2.59
Square	5	5	33	2.69	2.55	2.37	2.69
2-D nets							
Triangular net	6	3	18	2.73	2.34	2.29	2.54
Square net	4	4	20	2.69	2.03	1.90	2.34
Hexagonal net	3	3	12	2.69	1.46	1.38	2.00
1-D chains							
Zig-zag	4	3	8	2.76	1.61	1.59	2.09
Linear	2	2	4	2.74	0.92	0.89	1.33

[a] Coordination number (number of nearest neighbors).
[b] Number of shells out to cutoff ($2.25 \times r_{nn}$).
[c] Total number of atoms out to cutoff (including cenral atom).
[d] Nearest-neighbor distance.
[e] Equilibrium cohesive energy.
[f] Cohesive energy at fixed separation ($r_{nn} = r_{nn}$(fcc)).
[g] Cohesive energies calculated by Robertson *et al.* at fixed separation (31).
[h] N.B. U_R(fcc) is fixed at the room temperature value (3.36 eV), while U_e(fcc) is fixed at the 0 K value (3.39 eV).

Figure 4 shows the bct cell (shaded atoms) and the larger face-centered tetragonal (fct) cell (dotted lines), which is rotated by 45° with respect to the bct cell. In the bct definition, the bcc structure corresponds to $c/a = 1$, and fcc to $c/a = \sqrt{2}$. Thus, the conversion from fcc to bcc consists of a contraction parallel to the c axis, and an expansion isotropically parallel to the a and b axes. The variation of E_{coh} with c/a ratio, along the tetragonal Bain path, is shown in Fig. 5a for calcium (25, 37). The two minima correspond to the bcc and fcc allotropes. Our calculations predict an activation energy for the fcc → bcc transition of 0.0167 eV for Ca, with the activation energy in the reverse direction being 0.0014 eV (25). Figure 5b shows a contour plot of E_{coh} vs the reduced volume V/V_0 (where V_0 is the atomic volume of the fcc phase) and the c/a ratio. In agreement with experiment, only two minima are present on the centerd tetragonal surface. (It should be noted that calculations on copper by Morrison *et al.* indicate the presence of a metastable bct phase (38).)

6.3. *Thermodynamic Stabilities*

To calculate the thermodynamic stabilities of the fcc and bcc phases and the transition temperature (T_c) or pressure (P_c) it is necessary to calculate the phonon density of states (pDOS). Figure 6 shows a comparison of the calculated pDOS curves for fcc and bcc Ca (25). These curves were calculated by tetrahedral interpolation over a mesh of $17 \times 17 \times 17$ points (fcc) or $21 \times 21 \times 21$ points (bcc) in the the irreducible wedge (1/48th) of the Brillouin zone. These calculated DOS curves are in good agreement with those calculated by Heiroth *et al.* (39), using force constants derived by fitting experimental phonon dispersion curves.

By calculating the difference in Helmholtz free energy ($\Delta A = A$(bcc) $- A$(fcc)) as a function of temperature, a T_c value of 961 K was calculated for the transition from fcc to bcc Ca (25). The fact that the calculated T_c is higher than the experimental value (721 K) is probably due to our potential overestimating of the difference in cohesive energy

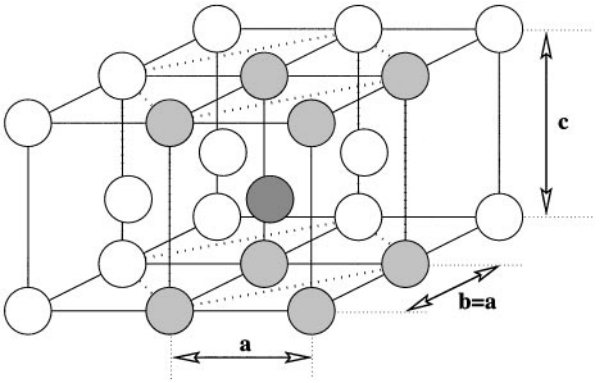

FIG. 4. Relationship between the body-centered tetragonal (shaded atoms) and face-centered tetragonal (dotted lines) unit cells.

between the fcc and the bcc structures. We have calculated that a decrease in ΔE_{coh} ($=E_{coh}(\text{fcc}) - E_{coh}(\text{bcc})$) from 0.014 to 0.011 eV would be sufficient to cause a decrease in T_c from 961 to 721 K (25) (assuming that all other contributions remain unchanged). If we bear in mind the sensitivity of the calculated T_c value to differences in U, our results are qualitatively satisfactory.

7. SURFACES: ENERGIES, RELAXATIONS, AND RECONSTRUCTIONS

The interlayer separations at metal surfaces differ from those of the bulk. This is known as surface relaxation, and it is common for the outer layer spacing of the fcc (110) and the bcc (100) surface to be less than the equivalent bulk spacing. Structural changes known as reconstructions, which involve movements in the surface plane as well as perpendicular to the surface plane, also occur on some surfaces, as the atoms find a lower energy configuration. For fcc and bcc metals, the surface energy (E_s) generally increases (i.e., the surface becomes less stable) as the coordination of the surface atoms decrease. In fcc solids, the order of E_s is (111) < (100) < (110), whereas in bcc solids it is (110) < (100) < (111), with the very open bcc(111) surface being particularly unfavorable. These surfaces are shown in Fig. 7.

Surface relaxations have been studied by optimizing the atomic positions in a slab of atoms having identical surfaces in both the $+z$ and $-z$ directions. For potentials derived with a cutoff of $3 \times r_{nn}$, the number of layers must be 9, 11, 15, 13, and 9 for fcc(111), fcc(100), fcc(110), bcc(100), and bcc(110) surfaces, respectively, in order that the center of the slab has effectively bulk character.

For full atom surfaces (i.e., surface layers having the same translational symmetry as the equivalent bulk) there are no net forces on atoms in the (x, y) directions so these unreconstructed surfaces need only be optimized in the z direction. We also examine the (1×2) and (1×3) reconstructions of the fcc(110) surface, in which there are missing rows of atoms relative to the unreconstructed fcc(110) surface. For these reconstructed surfaces there is both buckling and x, y displacement. All relaxed surface energies were calculated by minimizing the energy using a conjugate gradient routine (NAG routine e04dgf).

The surface energy is calculated as (33, 40):

$$E_s = \frac{NE_{coh} + V}{2A}, \qquad [23]$$

where V (the total potential energy of the slab) is a negative quantity, and E_{coh} (the bulk cohesive energy) is defined as a positive quantity. N is the number of atoms in the slab and A is the surface area of one side of the slab.

To illustrate our surface calculations we take as examples Pt and Pd (33). This pair of elements present a challenge, as

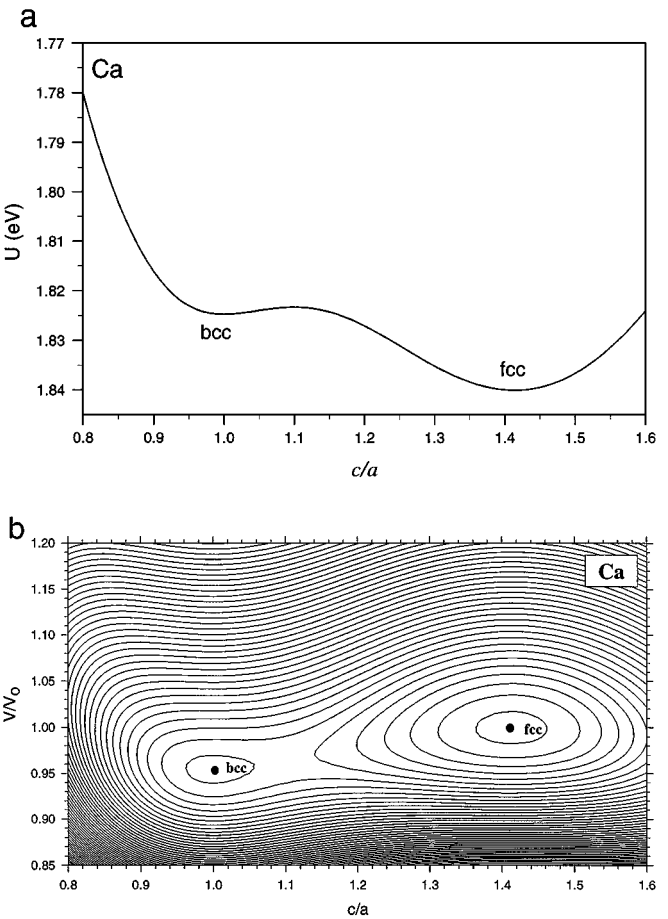

FIG. 5. The Bain tetragonal deformation path for calcium calculated using the dual-optimized MM Ca potential (25). (a) Variation of cohesive energy (U) with c/a ratio along the Bain path. (b) Contour plot of the centered tetragonal potential energy surface as a function of c/a and the reduced volume V/V_0, where V_0 is the volume (per atom) of the ground state fcc structure. The contour spacing is 0.003 eV.

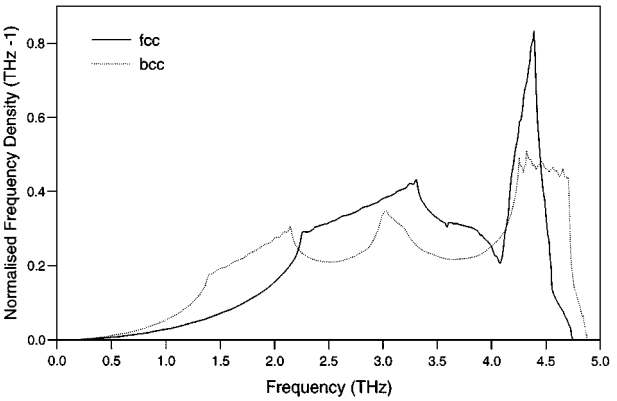

FIG. 6. Calculated phonon DOS for fcc (solid line) and bcc (dotted line) Ca (25).

TABLE 6
Relaxed Surface Energies E_s (meV/Å^2) for the Low Index Surfaces of fcc Pd and Pt

		(111)	(100)	(110)	$(1\times2)^a$	$(1\times3)^a$
Pd	**MM** (33)	**107.12**	**119.02**	**126.47**	**128.29**	**129.39**
	SC (42)	61.80	68.66	73.66	74.34	
	EAM (41)	67.04	72.22	77.40		
	Expt. (76)		**125.00**			
	Expt. (77)		**131.08**			
Pt	**MM** (33)	**131.90**	**152.28**	**161.79**	**161.36**	**161.57**
	SC (42)	55.18	63.67	67.66	66.66	
	EAM (41)	69.91	76.65	81.71		
	Expt. (76)		**155.40**			
	Expt. (77)		**159.00**			

[a] Reconstructed (110) surface.

Note. SC, Sutton–Chen potential; EAM, embedded atom method; Expt., experimental (average surface) extrapolated to 0 K. N.B. $1\,\mathrm{Jm^{-2}} = 1\,\mathrm{Nm^{-1}} = 10^3\,\mathrm{erg\,cm^{-2}} = 62.42\,\mathrm{meV/Å^2}$.

it is well known that Pt undergoes the (1×2) missing row reconstruction whereas Pd does not. This subtle balance between the (110) surface energy and the (1×2) missing row reconstruction is a stringent test for any potential (7). Our calculated surface energies are given in Table 6 together with a comparison with other calculated and experimental values. In agreement with experiment, we find the (1×2) reconstructed (110) surface of Pd to have a higher surface energy than the unreconstructed, whereas the (110) surface of Pt is found to reconstruct. Furthermore, the ratio of the surface energies of the (111) to the (110) surface is greater than $\sqrt{2/3}$ for Pd, indicating that the (110) surface is stable to the $(1\times\infty)$ reconstruction, whereas the ratio for Pt is less than $\sqrt{2/3}$, which signifies the preference for reconstruction of the Pt (110) surface (7).

The Pd (110) surface shows significant relaxation (see Table 7), and the contraction of the first interlayer spacing and expansion of the second are in excellent agreement with experiment. The Pd (100) surface also shows considerable movement. We do not reproduce the observed first interlayer expansion, but obtain a second interlayer contraction as observed experimentally; although we underestimate this movement, other theoretical works predict expansions (41). There is no consensus on the relaxations of the Pt (100) surface, and movements at the Pt (111) surface are small, as shown in Table 7.

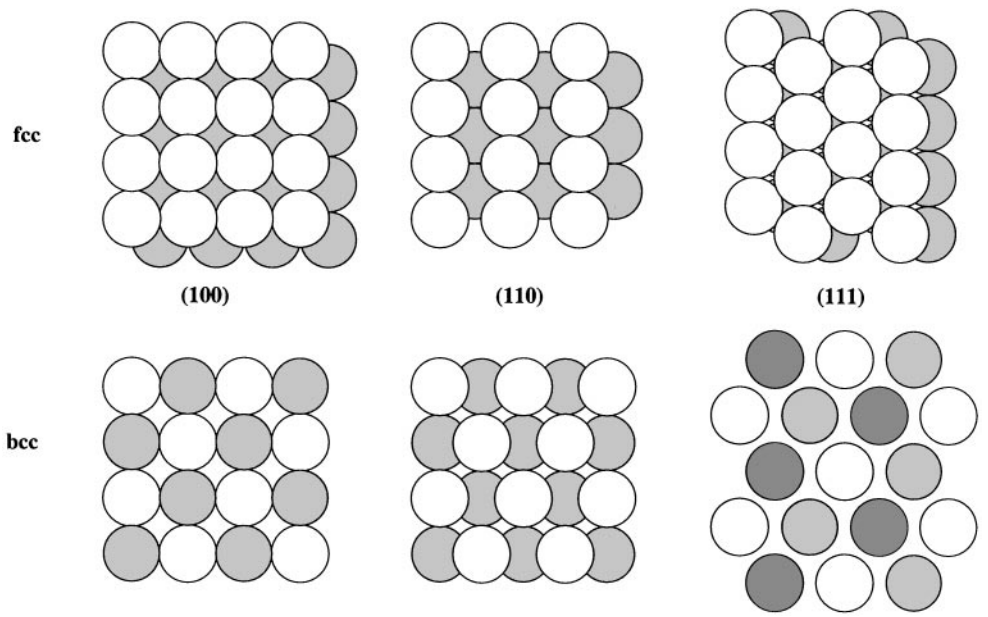

FIG. 7. Top views of the low-index surfaces of fcc and bcc metals. The shading represents atoms in different layers.

TABLE 7
Percentage Relaxation of the Three Outermost Interlayer Spacings of Unreconstructed fcc Pd and Pt Surfaces

	Surface	Δd_{12} (%)	Δd_{23} (%)	Δd_{34} (%)	Method		Surface	Δd_{12} (%)	Δd_{23} (%)	Δd_{34} (%)	Method
Pd	(111)	**−0.57**	**0.03**	**0.02**	**MM** (33)	Pt	(111)	**−0.75**	**0.04**	**0.01**	**MM** (33)
		−1.5			SC (42)			−3.3			SC (42)
		−2.40	0.20	−0.01	EAM (41)			−4.23	0.57	−0.07	EAM (41)
		0.0			AES, LEED (78)			1.0			LEED (79)
Pd	(100)	**−0.97**	**−0.03**	**0.02**	**MM** (33)	Pt	(100)	**−0.85**	**0.08**	**0.01**	**MM** (33)
		−2.3			SC (42)			−5.1			SC (42)
		−2.84	0.33	−0.02	EAM (41)			−5.55	0.87	0.13	EAM (41)
		3.0	−1		LEED (80)						
		2.25 ± 2.25			LEED (81)						
Pd	(110)	**−4.32**	**0.98**	**−0.36**	**MM** (33)	Pt	(110)	**−5.14**	**1.45**	**− 0.67**	**MM** (33)
		−5.8			SC (42)			−12.1			SC (42)
		−6.89	1.02	−0.04	EAM (41)			− 9.18	2.07	−0.51	EAM (41)
		−5.1 ± 1.5	1.9 ± 1.5		LEED (82)						
		−6.0 ± 2.0	1.0 ± 2.0		LEED (83)						

Note. Negative values are contractions in interlayer spacings compared to the bulk value. AES, Auger electron spectroscopy; LEED, low-energy electron diffraction. Other abbreviations are as in Table 6.

Table 8 compares some calculated and experimental parameters defining the relaxed geometries of the Pt (110)-(1 × 2) missing-row reconstruction, and these parameters are shown in Fig. 8. The MM potential underestimates the first and second interlayer relaxations, but correctly predicts both movements to be contractions. The third layer buckling has the correct sign, with the atoms under the missing row moving upward. Furthermore, the lateral displacement of the second layer atoms has the correct sign, with displacements being toward the missing row; the Sutton–Chen (42) and EAM (41) potentials do not give the correct sign of this displacement. However, we did not obtain any significant fourth layer pairing nor fourth layer buckling, whereas experiment shows that this does occur to a small extent.

TABLE 8
Distortions Accompanying the (1×2) Reconstruction of the Pt(110) Surface: Percentage Relaxation of the Two Outermost Interlayer Spacings (Δd_{ij}), the Pairing (p_2) and the Buckling (b_3), Relative to the Bulk Spacing of 1.3873 Å in z and 1.96 Å in x

	Pt (110)-(1 × 2)			
Method	Δd_{12}	Δd_{23}	p_2	b_3
Theory				
MM (33)	**− 4.47**	**−1.67**	**0.78**	**1.51**
SC (42)	−11.1	−3.7	−1.6	7.2
EAM (84)	−18.02	−5.05	−1.53	5.61
Experiment				
XRD (85)	−19.46	−7.93	2.55	—
LEED (86)	− 18.74	−12.97	3.57	23.09
MEIS (87)	−15.86	4.32	2.04	5.10

Note. Negative values are contractions in interlayer spacings and intralayer contractions, and a positive b_3 implies an upward displacement of third-layer atoms which have no first-layer atoms above them. XRD, X-ray diffraction; MEIS, medium-energy ion scattering. Other abbreviations are as in Tables 6 and 7.

8. SIMULATION OF LIQUIDS AND MELTING

As noted in the Introduction, melting is a strong indicator of the importance of many body contributions to the potential. This is true both for bulk melting and for surface melting, which is the appearance of a thin liquid-like layer on top of a solid surface below the bulk melting point. We illustrate our work by presenting results for Al, which has

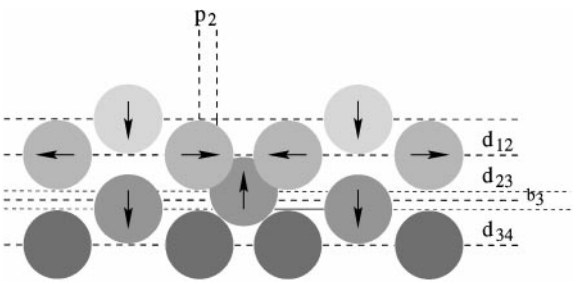

FIG. 8. Atomic displacements in the Pt (1 × 2) missing-row reconstructed (110) surface relative to ideal bulk positions (33).

been studied extensively by means of experiments as well as theory and computer simulation (see, for example, Refs. (43) and (44)). All authors report surface melting on Al(110) and no surface melting on Al(100); we confirmed these findings in our own study (45).

We simulated both bulk and surface melting using the standard Metropolis Monte Carlo simulation method (46, 47), with a maximum atom displacement chosen to give an acceptance rate of between 30 and 50%. Periodic boundary conditions have been used for surfaces and the bulk, the cell size being governed by the cutoff on which the potential is based. For these simulations a potential was optimized with a cutoff radius ($2.25 \times r_{nn}$) corresponding to interactions from 5 shells of atoms around any specified atom. We have confirmed that this cutoff gives very similar surface effects to those of the larger 10 shell cutoff and makes a significant saving in computer time.

For bulk melting *all* the atomic positions of atoms within a box of 200 atoms were optimized. The cell was constructed by taking 8 (100) layers of 5×5 atoms with a lattice spacing appropriate to the liquid density at the melting point.

To simulate surface melting, we allowed movement of a number of atoms on a fixed bulk structure. By virtue of our cutoff we were able to obtain convergent behavior of the first few layers by placing 12 (100) layers of 5×5 moving atoms and 14 (110) layers of 5×4 moving atoms, respectively, on top of 6 layers of fixed atoms. (The thickness of 12 (100) layers is approximately $8.5 \times r_{nn} = 24.8$ Å and that of 14 (110) layers is $7 \times r_{nn} = 20.5$ Å.) It was assumed that, since the atoms were allowed to move in the z-direction, the moving layers should expand to the volume appropriate for the density at melting. Following the approach of Allen and Tildesley (46), equilibration was monitored by recording the instantaneous values of the potential energy. The equilibration period was extended until this quantity ceased to show a systematic drift and started to oscillate about a steady mean value. Snapshots were recorded every 100 Monte Carlo cycles.

With these snapshots a number of parameters were monitored to track the "melting" of the lattice and subsequent progress to equilibrium:

- an order parameter (indicating how near the structure within a layer is to the ideal crystal structure),
- the radial distribution function, and
- the z-density profile.

The z-density profiles (which monitor the movement of atoms through the layers) were used to assign atoms to layers in order to calculate the order parameter and radial distribution function. The criterion for an atom to belong to a layer was that its z-coordinate should lie within the envelope of a peak (defining a specified layer at that temperature) in the profile.

It was found that both the bulk and the (100) surface behaved similarly with temperature. In both cases, the system gradually disordered up to our predicted T_m and then a sharp phase transition occurred as order was lost completely. In contrast, the order parameter for the (110) surface indicated a sudden disordering for the outer layers at temperatures lower than T_m. However, from the z-density profile plots it could be seen that vacancies and promotion of atoms to an overlayer had occurred at temperatures even lower than this phase change. This implies that the (110) surface goes through a solid-like structure (with vacancies and promotion of atoms to an overlayer) before becoming a lattice liquid. As the temperature increased to T_m a complete loss of order was apparent, indicative of a random liquid.

As the (100) surface disordered sharply, as in the bulk calculation, we concluded that surface melting on the (100) surface does not occur, but surface melting on the (110) surface *does* occur, approximately 200 K below the bulk melting point. These predictions are broadly in agreement with other studies of these surfaces.

Our predicted bulk melting temperature, from the (100) surface calculations, of $\approx 1275 \pm 25$ K is ≈ 350 K above the experimental value of 933 K. Our potential, which was based on room temperature data, therefore overestimated the melting point by 37%. Although this is much less than the overestimate ($\approx 200\%$) from two-body potentials alone, it indicates that in our two-body-plus-three-body formulation of the potential the extrapolation from room temperature to melting temperature conditions should be accompanied by a reduction of the energy scaling parameter by about 37%. This implies a reduction in cohesive energy by the same amount. To test this hypothesis, simulations were performed with the energy scaling factor D reduced by 37%. The lattice was then found to melt between 900 and 950 K.

This study of Al melting illustrated the ability of our many-body potential to reproduce the general features of surface and bulk melting, but it suggests strongly that our potentials, derived from room temperature data, will have to be adjusted, perhaps using a simple scaling rule, to give accurate melting temperatures.

9. CLUSTERS

There is considerable experimental and theoretical interest in the study of clusters, both in the gas phase and in the solid state (48, 49), due to the central position that they occupy between molecules and bulk materials and because of the interest in size-dependent properties (50).

Potentials for small clusters should be electronic state specific. For example, *ab initio* calculations on C_4 indicate that there are two low-lying structures which are very close in energy—a singlet planar rhombus and a triplet linear structure—though there is some disagreement as to which is actually the ground state (51). Clearly the potentials

required to accurately reproduce these minima on the singlet and triplet surfaces are quite different. However, potentials (such as ours) which are derived from crystalline solids will not be electronic state specific, as in the dissociation limit they will not satisfy the Wigner–Witmer electron correlation rules for breaking chemical bonds (52). We would, however, expect such potentials to be applicable to clusters which are sufficiently large that many electronic states are populated at the temperature at which the studies are made: certainly as the size of the cluster increases a potential deduced from bulk properties must become more valid. An important feature of our potentials is that, although derived from bulk data, they have been shown to give a good representation of surface properties, and, as even large clusters have a substantial fraction of their atoms at or near the surfaces, we expect our potentials to be reliable for cluster studies.

MM potentials have been used to study the structures, growth, and dynamics of clusters formed from a range of metallic and nonmetallic elements, using the program CLUSPRO (53). Examples of the application of the MM potential to clusters are described in Sections 9.2 and 9.3 The potentials used in these calculations are given in the cited papers, and many of them are listed in Tables 2 and 3.

9.1. Cluster Energetics

Within the two-plus-three-body MM model, the total potential energy of an N-atom cluster is given by summing over all pairs and triples in the cluster

$$V_{\text{clus}} = \sum_{i}^{N-1} \sum_{j>i}^{N} V_{ij}^{(2)} + \sum_{i}^{N-2} \sum_{j>i}^{N-1} \sum_{k>j}^{N} V_{ijk}^{(3)}, \qquad [24]$$

where, generally, only terms with all distances within the cutoff of the potential are included in the summation. The average binding energy (i.e., the binding energy per atom) is a positive quantity, which is defined as

$$E_{\text{b}} = \frac{-V_{\text{clus}}}{N}. \qquad [25]$$

The second difference in the binding energy is defined as

$$D_2(N) = 2E_{\text{b}}(N) - E_{\text{b}}(N-1) - E_{\text{b}}(N+1). \qquad [26]$$

A peak in $D_2(N)$ indicates an enhanced stability of a cluster of N atoms with respect to its heavier and lighter neighbors, which either may arise from the evaporative cooling of the clusters or may be due to the existence of quasi-equilibrium conditions in the cluster beam nozzle during cluster formation (54). It is this quantity, rather than the binding energy (E_{b}), that is generally correlated with experimental mass spectral intensities.

The average binding energy tells us nothing about the relative strength of binding of the various inequivalent atoms in the cluster. To investigate how the binding energy varies for atoms in different environments (i.e., symmetry-inequivalent atoms) it is necessary to calculate partial binding energies. The binding energy of a specific atom (i) in a cluster is given by (55):

$$\varepsilon_{\text{b}}(i) = -\left(\frac{1}{2}\sum_{j}{}' V_{ij}^{(2)} + \frac{1}{6}\sum_{j}{}' \sum_{k\neq j}{}' V_{ijk}^{(3)}\right), \qquad [27]$$

where the prime indicates summation over all atoms except i. The average binding energy is regained as

$$E_{\text{b}} = \frac{\sum_i \varepsilon_{\text{b}}(i)}{N}. \qquad [28]$$

As their environments are identical, the ε_{b} values for all symmetry-equivalent atoms are also identical. This is particularly useful for geometric shell clusters, where a set of symmetry-equivalent atoms is known as a geometric subshell and the partial binding energy is known as the subshell binding energy (55). If there are n_k atoms in subshell k, the average binding energy can be obtained by summing over the subshell binding energies (i.e., the partial binding energy of any atom in the subshell) $\varepsilon_{\text{b}}(k)$ (55):

$$E_{\text{b}} = \frac{\sum_k n_k \varepsilon_{\text{b}}(k)}{N} \qquad [29]$$

This principle has been utilized to speed up the radial optimization of shell clusters within the CLUSPRO program (56).

9.2. Full Geometry Optimization of Small Clusters

It is well known that finding the global minimum on a multi-dimensional PES is a difficult problem (57). This is because the number of structurally distinct isomers (minima) increases quasi-exponentially with increasing nuclearity, due to the high dimensionality ($3N-6$) of configuration space. Hence, not only is it necessary to develop a PEF which provides a good description of clusters over a wide range of configuration space, it is also essential to employ a suitable method for searching the PE surface.

9.2.1. Random search method. The simplest, unbiased method for finding minima on a PES is to perform a large number of searches from random starting points. In the random search approach for metal clusters, each starting structure is generated by picking N sets of coordinates at random, subject to the conditions that (58): the atoms lie

within a sphere of radius $R_{clus} = r_{nn} \times N^{1/3}$; no two atoms can be closer than $r_{min} = 0.7 \times r_{nn}$; and the shortest distance between an atom and its neighbors cannot be greater than $r_{max} = 1.3 \times r_{nn}$ (r_{nn} is the nearest-neighbor distance in the bulk solid). The first condition ensures that the cluster volume scales (correctly) as N and also that the starting geometries tend to be pseudospherical and relatively close packed. The second condition precludes starting geometries which are too compressed, and hence very high in energy, and the third condition prevents initial geometries in which one or more atoms are not connected to the remainder of the cluster.

The potential energy and the average binding energy are calculated for the initial, unrelaxed cluster (Eqs. [24] and [25]); the cluster potential energy is then minimized by relaxing the cluster geometry, using the quasi-Newton NAG routine e04kaf or the conjugate gradient algorithm e04dgf (8), both of which which utilize analytical first derivatives of the potential. The average binding energy of the relaxed cluster, corresponding to a local minimum on the PES, is then stored. Since both these routines can converge to saddle points as well as minima, analytic first and second derivatives of the potential are also used to calculate cluster vibrational frequencies, the order of a stationary point being equal to the number of imaginary frequencies.

9.2.2. Other minimization techniques. The crude random search method often requires a large number of searches to find the GM on the cluster PES, even for as few as 20 atoms. As the number of isomers increases quasi-exponentially with N, the number of searches required increases dramatically and the search procedure becomes extremely time consuming. Also, the confidence with which we can say that the global minimum has actually been found decreases with increasing N. A number of other methods for searching a cluster PES surface for minima are currently available: Monte Carlo and molecular dynamics methods (usually involving simulated annealing) (59), eigenvector following (60), basin hopping (61), and methods based on genetic algorithms (62). Recently, Monte Carlo simulated annealing (58), molecular dynamics simulated annealing (56) and genetic algorithm codes have been written for finding the global minima of MM clusters (63, 64).

9.2.3. Small carbon clusters. The quartic MM potential for carbon listed in Table 3 was used to calculate the relative stabilities of small carbon clusters with varying topologies (17). It was found that the binding energies (per atom) of linear chains increase monotonically with the number of atoms whereas cyclic clusters display a maximum binding energy for six-membered rings. Full optimization of carbon clusters with up to 22 atoms (using a random search algorithm) showed a preference for three-dimensional structures with five- and six-membered rings, with all atoms at least three-connected. Hobday and Smith subsequently performed a search for the lowest energy isomers of small carbon clusters (bound with the MM potential) using a genetic algorithm (65). In a number of cases, they found lower energy isomers than in our previous paper (17), though we have recently found (using our own genetic algorithm (63)) some isomers which are more stable than those reported by Hobday and Smith.

In our original paper (17), we performed local minimization studies on fullerene cage clusters and found that the binding energy increased fairly monotonically with cluster size, in the region $N = 20$–82, although I_h–C_{60} and D_{5h}–C_{70} were found to be local maxima in binding energy. The calculated binding energy of C_{60} (7.25 eV) is in good agreement with experimental measurements (7.063 eV (66)).

9.2.4. Small aluminium clusters. The random search method has been used to find the global minima for aluminum clusters with up to 20 atoms, bound by the cubic MM potential listed in Table 2 (58). The structures corresponding to these global minima are shown in Fig. 9, and their average binding energies are plotted in Fig. 10a. After a rapid initial increase, the binding energy converges slowly toward the bulk value ($E_{coh} = 3.39$ eV) for fcc Al. An important feature of this graph is the small peak at $N = 13$, which corresponds to a region of enhanced stability. Such regions are more evident when the second difference in the binding energy is plotted against N, as in Fig. 10b. This plot shows that there are pronounced peaks in $D_2(N)$ at $N = 4$, 6, and 13 and a small peak at 19. This is in marked contrast to the $D_2(N)$ graphs for Ca and Sr (where there are significant peaks at $N = 7$ and $N = 19$ (55)) and may indicate the reduced stability of five-fold symmetric icosahedral packing in Al compared to Ca and Sr and a preference for fragments based on fcc packing, such as the octahedron for $N = 6$. It is interesting to note that the mass spectroscopic

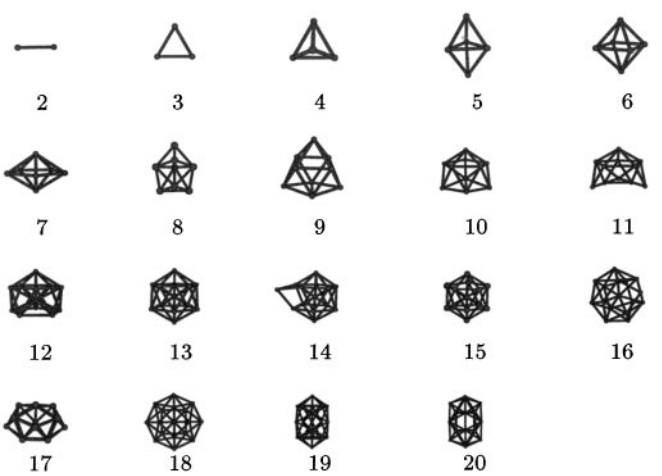

FIG. 9. Global minima found for Al_2–Al_{20} (modeled with the MM potential for Al) using the random search method (58).

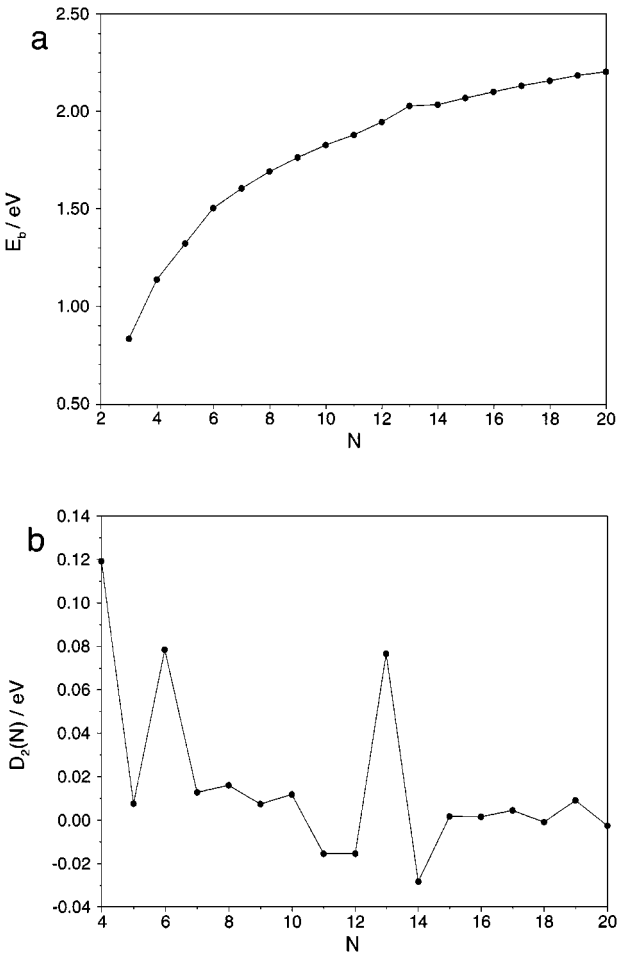

FIG. 10. Stabilities of small Al clusters as a function of size (N) calculated using the MM Al potential (58). (a) Binding energies (E_b) calculated for the global minima of Al_3–Al_{20}. (b) Second difference (D_2) in calculated binding energies for the global minima of Al_4–Al_{20}.

measurements of Martin and co-workers indicate that large Al clusters (of hundreds or thousands of atoms) grow as fcc octahedra, while clusters of Ca grow as noncrystalline icosahedra up to at least 5000 atoms (67).

9.3. Radial Optimization of Large Geometric Shell Clusters

For larger clusters (with up to 1000 atoms) we have investigated geometric (or polyhedral) shell structures generated from the bulk cubic solids (diamond (d), simple cubic (sc), bcc and fcc) and also for some noncubic structures, such as icosahedral (ico) and decahedral (dec), with the radius of each concentric shell being optimized independently. These radially optimized shell structures can subsequently be fully optimized by minimizing their energy with respect to cartesian displacement of all atoms, as described above for small clusters.

In CLUSPRO (53, 56), shell clusters are generated by scaling the coordinates of the polyhedral clusters so that the shortest interatomic distance in the cluster, r_{nn}(clus), is equal to the nearest-neighbor distance in the most stable bulk structure, r_{nn}(bulk). A two-stage optimization procedure is adopted to radially relax geometric shell clusters (55). Such radial relaxation leaves the point group of the cluster unchanged.

(i) *Partial radial relaxation* for an S-shell cluster is achieved by minimizing the average cluster binding energy as a function of a set of S scaling factors which define how expanded or contracted the complete geometric shells are with respect to the starting configuration. Minimization is performed using the conjugate gradient NAG routine e04ucf. This is a relatively fast procedure, as the number of variables (scaling factors) is small.

(ii) *Full radial relaxation* is accomplished by taking the partially relaxed clusters and allowing the geometric subshells to move independently of each other (by assigning them separate scaling factors). Energy minimization is again achieved using the conjugate gradients algorithm. In this final stage, tangential as well as purely radial motion has to be allowed for atoms which do not lie on symmetry axes (56). Since point group symmetry must still be preserved, symmetry-equivalent atoms (subshells) are constrained to move in symmetry-related ways.

The calculation of the cluster potential energy and the first derivatives of the potential have been greatly accelerated by introducing a cutoff into the two- and three-body summations and performing these summations about a single atom in each subshell, making use of Eqs. [27] and [29] (56).

9.3.1. Magic numbers for geometric shell metal clusters. There are a variety of structures which may be postulated for geometric shell metal clusters, such as the cuboctahedron (cub), a fragment of the fcc lattice; the icosahedron (ico); the truncated decahedron (dec); and the rhombic dodecahedron (rho), a fragment of the bcc lattice. The magic number (i.e., total number of atoms N) for a cluster consisting of T complete polyhedral shells around a central atom has been derived by Martin (67):

$$N = \tfrac{1}{3}(10T^3 + 15T^2 + 11T + 3), \qquad [30]$$

for cub, ico, and dec shell clusters (e.g., $N = 13$, 55, 147, 309 and 561 for $T = 1$, 2, 3, 4, and 5). For rho shell clusters, the magic numbers are given by

$$N = 4T^3 + 6T^2 + 4T + 1 \qquad [31]$$

(e.g., $N = 15$, 65, 175, 369, and 671 for $T = 1$, 2, 3, 4, and 5). The outer shells of 5-shell ico, dec, cub, and rho clusters are shown in Fig. 11.

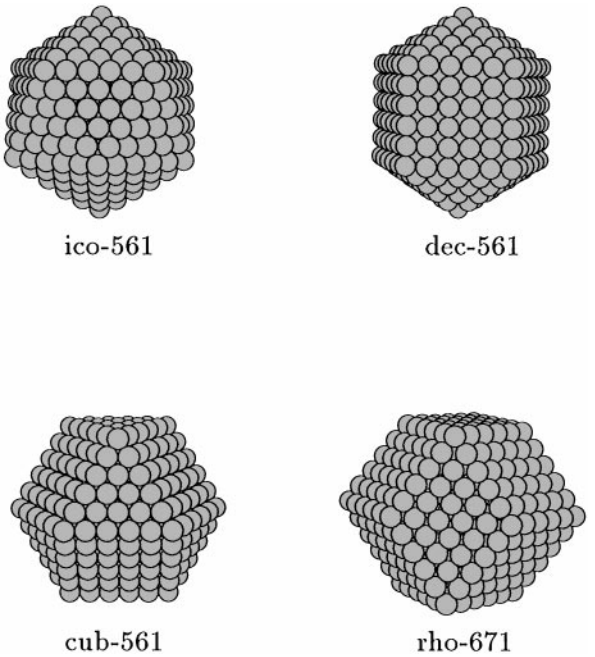

FIG. 11. Representation of the outer shells of some five-shell polyhedral clusters. The numbers indicate the total number of atoms in each cluster.

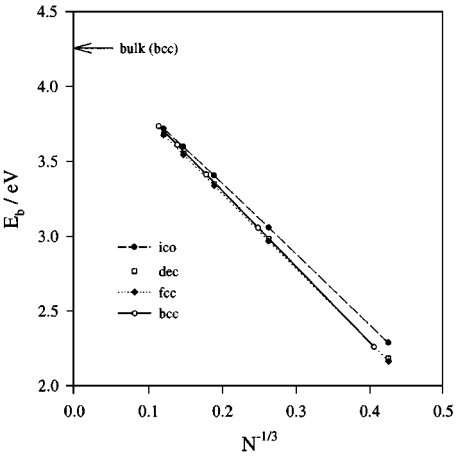

FIG. 12. Plot of binding energy (E_b) against $N^{-1/3}$ for radially optimized shell clusters Fe_N calculated using the dual-optimized MM Fe potential (69). The cohesive energy of bulk α-Fe (bcc: 4.28 eV) is indicated by the arrow at left.

Following Northby *et al.* the binding energy of a pseudospherical N-atom cluster can be written as a polynomial in $N^{-1/3}$ (68):

$$E_b = \frac{-V_{tot}}{N} = a + bN^{-1/3} + cN^{-2/3} + dN^{-1}. \quad [32]$$

Constant a represents the bulk or volume contribution to the cluster potential energy (cluster volume $V_c \propto N \propto R_c^3$, where R_c is the radius of the cluster). b represents the surface or area contribution (cluster surface area $A_c \propto R_c^2 \propto N^{2/3}$), c is the edge or length contribution (edge length $L_c \propto R_c \propto N^{1/3}$); and d is the vertex contribution.

9.3.2. Geometric shell iron clusters. The quartic MM potential (Table 3) for iron (22) was used to calculate the stabilities and relaxations of geometric shell iron clusters with up to 5 shells (69). Figure 12 is a plot of binding energy against $N^{-1/3}$ and shows that the stability order in this size regime is ico > rho > dec > cub. The relative stabilization of icosahedral structures is consistent with the structures obtained from full geometry optimization of small clusters (69).

The coefficients obtained by fitting the binding energies to Eq. [32] are listed in Table 9. The stability in the infinite cluster limit (as measured by a) was found to be ico ≈ dec < cub < rho, which is to be expected, since the MM potential for Fe was simultaneously optimized to lattice dynamical and structural data for both the α and the γ phases (22). The a values for rho and cub shell clusters were both found to be within 0.2% of the respective cohesive energies (E_{coh}(bcc) and E_{coh}(fcc)) as calculated by the program SOLIDS. The values of b were found to be negative, with the magnitudes in the order rho ≈ cub > dec > ico, reflecting increasing surface stability on going from rho to ico clusters, since ico shell clusters are characterized by 20 close-packed (111)-type faces.

Figure 12 shows that rho clusters are preferred over cub or dec geometries (i.e., they have higher binding energies) even at low nuclearities. From the fitting coefficients in Table 9, the crossover from ico to rho shell clusters is predicted to occur at around 2000 atoms (69). Of course, for specific closed geometric shells, the magic numbers for ico and rho clusters are different, so it may be possible for an alternation of structure as a function of cluster nuclearity, for iron clusters. Indeed, mass spectroscopic studies by Pellarin *et al.* indicate that, whereas for cobalt and nickel

TABLE 9

Fitting Parameters (eV) for Eq. [32] for Icosahedral (ico), Decahedral (dec), Cuboctahedral (cub), and Rhombic Dodecahedral (rho) Fe Clusters, with Binding Energies Calculated Using the Quartic MM Potential for Fe (69)

Parameter	ico	dec	cub	rho
a	4.248	4.250	4.255	4.284
b	−4.180	−4.454	−4.615	−4.635
c	−1.761	−2.085	−1.641	−1.695
d	1.755	2.673	2.183	2.021

clusters, intensity variations in the mass spectra can be explained in terms of icosahedral shell structures, in the case of iron there is no simple pattern in the mass spectrum (70). Analysis of the published mass spectrum for iron clusters reveals that a number of the features (sharp intensity variations) correspond closely to predicted magic numbers for complete icosahedral shell clusters, while others are close to the values expected for bcc-like rhombic dodecahedral clusters (50).

9.3.3. Shell-like silicon clusters. Shell-like clusters have also been studied for silicon, using the quartic MM potential listed in Table 3 (71). In this study, a shell was defined as a group of symmetry-equivalent atoms lying on a sphere at a certain distance (radius) from a central atom, and the optimized shell structure was obtained by varying the radii of the shells independently. As an example, a diamond-like Si_{47} cluster consists of concentric shells of 4, 12, 12, 6, and 12 atoms around the central atom, and the whole cluster (which may be represented as 1:4:12:12:6:12) possesses T_d symmetry. The largest diamond shell cluster that we studied has 357 atoms (19 shells) and a binding energy (4.63 eV) which is still short of the bulk Si (diamond) cohesive energy of 4.72 eV, because, even for this relatively large cluster, approximately one-third of the atoms are on the surface (i.e., they have unsaturated valencies or dangling bonds).

Figure 13 shows the binding energies of radially relaxed geometric shell Si_N clusters ($N \leq 100$) derived from the cubic solids. In this range, the sc and bcc clusters are generally more stable (i.e., have higher binding energies) than diamond-like clusters. In fact, even fcc Si_{43} has a higher binding energy than diamond clusters of comparable size, and diamond clusters only become preferred well above 100 atoms. Our results are consistent with the semi-empirical (SINDO1) calculations of Kupka and Jug (72). We also found a general upward trend in binding energy for all the cubic structures, which is to be expected since the average number of dangling bonds per atom decreases as the ratio of surface to bulk atoms decreases. Superimposed on the general increase in binding energy, there are a number of peaks of stability corresponding to magic number clusters. The most prominent of these is the three-shell 27 atom sc cluster (inset in Fig. 13) which has a binding energy of 4.14 eV/atom and is the most stable shell structure up to 55 atoms. This structure is composed of many square rings and has a number of atoms with coordination numbers higher than four. The high stability of sc Si_{27} is consistent with the MM results for small Si clusters, where highly connected structures with four-membered rings were found to be preferred (71). Finally, it should be noted that *ab initio* DFT calculations by Röthlisberger *et al.* indicate that Si clusters with between 30 and 40 atoms have cores which are indeed more highly connected than in the diamond structure (73).

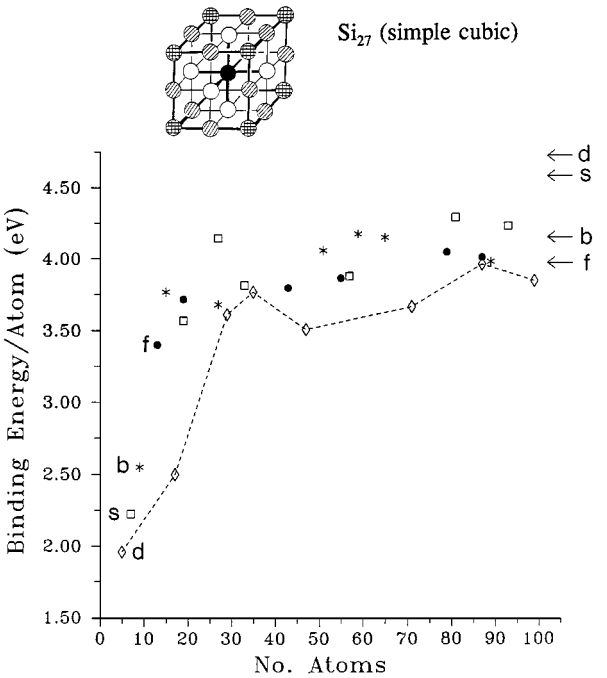

FIG. 13. Plot of calculated binding energy as a function of number of atoms for radially optimized silicon shell clusters (modeled with the MM Si potential) derived from the diamond (d), simple cubic (s), bcc (b), and fcc (f) solids (71). The bulk cohesive energies are indicated by the arrows at right. (Inset: The simple cubic Si_{27} cluster is the most stable shell structure up to 55 atoms.)

10. SUMMARY

It has been shown that MM potentials, based on two-body and three-body terms, can be derived for a wide range of elemental solids for which phonon data are available. We have encountered few difficulties in finding potentials for simple metals and transition metals, with bcc or fcc structures. Potentials have also been derived for the group 14 elements having diamond structures, although the fitting to the phonon dispersion curves at the Brillouin zone boundaries is not quite as good as for the metals; there is some indication that terminating the potential at the three-body term is less satisfactory for group 14 elements than for metals.

The parameters (coefficients) of the three-body terms show broadly similar patterns among families of elements. For example, the potentials for Si and Ge are quite similar (but noticeably different from the carbon potential); likewise those for the alkali metals and the coinage (noble) metals are closely related within each group. This property suggests that it may be possible to find simple combining rules for alloys and intermetallics, at least where the elements are within the same family; this is currently being explored for Si–Ge and Cu–Au alloys.

The MM potential, when determined from data on one solid phase, has been shown to give a good description of

the energies and structures of other 3-D, 2-D, and 1-D lattices; particularly noteworthy is the fact that our Al potential, when applied to other structures, gives results in good agreement with the results of direct electronic structure calculations. However, we have also shown that we can simultaneously fit to data from more than one solid phase, particularly data for fcc and bcc phases, and we have shown that both the Bain transition path between these two structures and the thermodynamic stabilities of the phases can be reproduced.

An important feature of the MM potential is that it has been shown to reproduce surface properties for a wide range of systems; in particular it gives good surface contractions for unreconstructed surfaces and reproduces the experimentally observed (1×2) missing row reconstructions of the (110) surfaces of fcc Au and Pt. Because the MM potential reproduces both bulk and surface properties, we believe it is well placed to study clusters, and our calculations on these have been extensive. Results for small clusters, where full geometry optimizations have been carried out, have shown that in many cases our potentials predict minimum energy structures which are very close to the global minima derived by *ab initio* calculations, at a fraction of the computational cost. Radial optimization studies of larger geometric shell clusters give good agreement with experimental studies of cluster structure and stability.

We have made only one extensive study of melting and that has been with the Al potential. This study suggests that our potentials, which are generally based on room temperature data, will have to be scaled to give good melting temperatures. This is not unexpected because the continuum of electronic levels in metals makes it unavoidable that any Born–Oppenheimer potential would have a significant temperature dependence. Perhaps the most important point established from this melting study is that our potential has a sufficiently simple analytic form that it can be used for MC or MD simulations without too great a demand on computing resources; although three-body terms have to be summed, their functional form does not make exessive computational demands.

Taking all of these facts into consideration, we claim that the MM potential has been shown to be at least as good as any other candidates for general, global empirical potentials; indeed, we know of no other potential which has been applied successfully over such a large range of elements.

ACKNOWLEDGMENTS

The authors thank members of the Sussex "potential" group, past and present, who have been involved in the work reported in this review and whose names can be found in the many publications cited herein. We acknowledge in particular the many important contributions made by Drs. B. R. Eggen, J. Y. Fang, and J. E. Hearn (Sussex), and Mrs. L. D. Lloyd and Mr. N. T. Wilson (Birmingham). H.C. thanks the Royal Society for the award of a Dorothy Hodgkin Research Fellowship. Much of the work reported in this review was carried out while R.L.J. was a Royal Society University Research Fellow at the University of Sussex.

REFERENCES

1. M. Rigby, E. B. Smith, W. A. Wakeham, and G. C. Maitland, "The Forces between Molecules," Clarendon Press, Oxford, 1986.
2. F. Ercolessi, M. Parrinello, and E. Tosatti, *Philos. Mag. A* **58,** 213 (1988).
3. V. Vitek, *MRS Bull.* **21,** 20 (1996).
4. I. J. Robertson, V. Heine, and M. C. Payne, *Phys. Rev. Lett.* **70,** 1944 (1993).
5. J. N. Murrell, S. Carter, S. C. Farantos, P. Huxley, and A. J. C. Varandas, "Molecular Potential Energy Functions," Wiley, Chichester, 1984.
6. R. S. Leigh, B. Szigeti, and V. K. Tewary, *Proc. Roy. Soc. London A* **320,** 505 (1971).
7. K. D. Hammonds, *Mol. Phys.* **81,** 227 (1994).
8. "NAG Fortran Library Manual," 16th ed., Numerical Algorithms Group Ltd., Oxford, 1993.
9. J. N. Murrell and J. A. Rodriguez-Ruiz, *Mol. Phys.* **71,** 823 (1990).
10. A. Al-Derzi, R. L. Johnston, J. N. Murrell, and J. A. Rodriguez-Ruiz, *Mol. Phys.* **73,** 265 (1991).
11. F. H. Stillinger and T. A. Weber, *Phys. Rev. B* **31,** 5262 (1985).
12. J. Tersoff, *Phys. Rev. Lett.* **56,** 632 (1986).
13. R. Biswas and D. R. Hamann, *Phys. Rev. B* **36,** 6434 (1987).
14. M. T. Yin and M. L. Cohen, *Phys. Rev. B* **26,** 5668 (1982).
15. M. T. Yin and M. L. Cohen, *Phys. Rev. Lett.* **50,** 2006 (1983).
16. B. R. Eggen, R. L. Johnston, S. Li, and J. N. Murrell, *Mol. Phys.* **76,** 619 (1992).
17. B. R. Eggen, R. L. Johnston, and J. N. Murrell, *J. Chem. Soc. Faraday Trans.* **90,** 3029 (1994).
18. I. Marone, "The Application of Many-Body Potential Energy Functions to Diamond Silicon," D.Sc. thesis, Universidade Estadual de Campinas, Brazil, 1997.
19. J. Donohue, "The Structures of the Elements," 2nd ed., Wiley, New York, 1974.
20. W. Maysenholder, S. G. Louie, and M. L. Cohen, *Phys. Rev. B* **31,** 1817 (1985).
21. L. Vocadlo, G. A. deWijs, G. Kresse, M. Gillan, and G. D. Price, *Faraday Discuss.* **106,** 205 (1997).
22. F. Gao, R. L. Johnston, and J. N. Murrell, *J. Phys. Chem.* **97,** 12073 (1993).
23. A. T. Paxton, M. Methfessel, and H. M. Polatoglou, *Phys. Rev. B* **41,** 8127 (1990).
24. M. I. Baskes, *Phys. Rev. B* **46,** 2727 (1992).
25. J. E. Hearn, R. L. Johnston, S. Leoni, and J. N. Murrell, *J. Chem. Soc. Faraday Trans.* **92,** 425 (1996).
26. H. Cox, X. Liu, and J. N. Murrell, *Mol. Phys.* **93,** 921 (1998).
27. J. W. Lynn, H. G. Smith, and R. M. Nicklow, *Phys. Rev. B* **8,** 3493 (1973).
28. J. Y. Fang, R. L. Johnston, and J. N. Murrell, *Mol. Phys.* **78,** 1405 (1993).
29. J. Y. Fang, R. L. Johnston, and J. N. Murrell, *J. Chem. Soc. Faraday Trans.* **89,** 1659 (1993).
30. J. N. Murrell and R. E. Mottram, *Mol. Phys.* **69,** 571 (1990).
31. I. J. Robertson, M. C. Payne, and V. Heine, *Europhys. Lett.* **15,** 301 (1991).
32. R. L. Johnston and J.-Y. Fang, *J. Chem. Phys.* **97,** 7809 (1992).
33. H. Cox, *Surf. Sci.* **397,** 374 (1998).
34. I. J. Robertson, D. I. Thomson, V. Heine, and M. C. Payne, *J. Phys. Condens. Matter* **46,** 9963 (1994).
35. E. C. Bain, *Trans. Am. Inst. Min. Eng.* **70,** 25 (1924).

36. D. A. Porter and K. E. Easterling, "Phase Transformations in Metals and Alloys," 2nd ed., Chapman & Hall, London, 1992.
37. K. M. Andersson, R. L. Johnston, and J. N. Murrell, *Phys. Rev. B* **49,** 3089 (1994).
38. I. A. Morrison, M. H. Kang, and E. J. Mele, *Phys. Rev. B* **39,** 1575 (1989).
39. M. Heiroth, U. Buchenau, and H. R. Schober, *Phys. Rev. B* **34,** 6681 (1986).
40. J. Uppenbrink, R. L. Johnston, and J. N. Murrell, *Surf. Sci.* **304,** 223 (1994).
41. J. Cai and Y. Y. Ye, *Phys. Rev. B* **54,** 8398 (1996).
42. B. D. Todd and R. M. Lynden-Bell, *Surf. Sci.* **281,** 191 (1993).
43. H. Dosch, *Physica B* **198,** 78 (1994).
44. A. Denier van der Gon, D. Frenkel, J. W. M. Frenken, R. J. Smith, and P. Stolze, *Surf. Sci.* **256,** 385 (1991).
45. H. Cox, R. L. Johnston, and J. N. Murrell, *Surf. Sci.* **373,** 67 (1997).
46. M. P. Allen and D. J. Tildesley, "Computer Simulation of Liquids," Clarendon Press, Oxford, 1989.
47. D. W. Heermann, "Computer Simulation Methods," Springer-Verlag, Berlin, 1990.
48. H. Haberland (Ed.), "Clusters of Atoms and Molecules," Springer-Verlag, Berlin, 1994.
49. T. P. Martin (Ed.), "Large Clusters of Atoms and Molecules," Kluwer, Dordrecht, 1996.
50. R. L. Johnston, *Philos. Trans. R. Soc. London Ser A* **356,** 211 (1998).
51. W. Weltner, Jr. and R. J. van Zee, *Chem. Rev.* **89,** 1713 (1989).
52. E. P. Wigner and E. E. Witmer, *Z. Phys.* **51,** 859 (1928).
53. R. L. Johnston and N. T. Wilson, University of Birmingham, 1997.
54. W. A. de Heer, *Rev. Mod. Phys.* **65,** 611 (1993).
55. J. E. Hearn and R. L. Johnston, *J. Chem. Phys.* **107,** 4674 (1997).
56. N. T. Wilson and R. L. Johnston, in preparation (1999).
57. R. S. Berry and R. E. Kunz, *in* "Large Clusters of Atoms and Molecules" (T. P. Martin, Ed.), p. 299. Kluwer, Dordrecht, 1996.
58. L. D. Lloyd and R. L. Johnston, *Chem. Phys.* **236,** 107 (1998).
59. S. Kirkpatrick, C. D. Gelatt, and M. P. Vecchi, *Science* **220,** 671 (1983).
60. D. J. Wales, *J. Chem. Phys.* **101,** 3750 (1994).
61. D. J. Wales and J. P. K. Doye, *J. Phys. Chem. A* **101,** 5111 (1997).
62. D. M. Deaven, N. Tit, J. R. Morris, and K. M. Ho, Chem. *Phys. Lett.* **256,** 195 (1996).
63. F. R. Manby, R. L. Johnston, and C. Roberts, *MATCH* **38,** 111 (1998).
64. C. Roberts, R. L. Johnston, and N. T. Wilson, in preparation (1999).
65. S. Hobday and R. Smith, *J. Chem. Soc. Faraday Trans.* **93,** 3919 (1997).
66. H.-D. Beckhaus, C. Rüchardt, M. Kao, F. Diederich, and C. S. Foote, *Angew. Chem. Int. Ed. Engl.* **31,** 63 (1992).
67. T. P. Martin, *Phys. Rep.* **273,** 199 (1996).
68. J. A. Northby, J. Xie, D. L. Freeman, and J. D. Doll, *Z. Phys. D* **12,** 69 (1989).
69. N. A. Besley, R. L. Johnston, A. J. Stace, and J. Uppenbrink, *J. Mol. Struct. THEOCHEM* **341,** 75 (1995).
70. M. Pellarin, B. Baguenard, J. L. Vialle, J. Lermé, M. Broyer, J. Miller, and A. Perez, *Chem. Phys. Lett.* **217,** 349 (1994).
71. S. Li, R. L. Johnston, and J. N. Murrell, *J. Chem. Soc. Faraday Trans.* **88,** 1229 (1992).
72. H. Kupka and K. Jug, *Chem. Phys.* **130,** 23 (1989).
73. U. Röthlisberger, W. Andreoni, and M. Parrinello, *Phys. Rev. Lett.* **72,** 665 (1994).
74. H. Cox, unpublished work.
75. H. Cox, R. L. Johnston, and A. Ward, *J. Phys.: Condens. Matter* **10,** 9419 (1998).
76. W. R. Tyson and W. A. Miller, *Surf. Sci.* **62,** 267 (1977).
77. A. R. Miedema, *Z. Metallkd.* **69,** 287 (1978).
78. Y. Kuk, L. C. Feldman, and P. J. Silverman, *Phys. Rev. Lett.* **50,** 511 (1983).
79. D. L. Adams and H. B. Nielsen, *Phys. Rev. B* **20,** 4789 (1979).
80. J. Quinn, Y. S. Li, D. Tian, H. Li, F. Jona, and P. M. Marcus, *J. Phys. C* **18,** 4069 (1985).
81. R. J. Behm, K. Christmann, G. Ertl, and M. A. van Hove, *J. Chem. Phys.* **73,** 2984 (1980).
82. M. Skottke, R. J. Behm, G. Ertl, V. Penka, and W. Moritz, *J. Chem. Phys.* **87,** 6191 (1987).
83. R. D. Diehl, M. Lindroos, A. Kearsley, C. J. Barnes, and D. A. King, *J. Phys. C* **18,** 4069 (1985).
84. S. M. Foiles, *Surf. Sci.* **191,** L779 (1987).
85. E. Vlieg, I. K. Robinson, and K. Kern, *Surf. Sci.* **233,** 248 (1990).
86. E. C. Sowa, M. A. van Hove, and D. L. Adams, *Surf. Sci.* **199,** 174 (1988).
87. P. Fenter and T. Gustafsson, Phys. *Rev. B* **38,** 10197 (1988).